Journal of Molecular Structure 1353 (2026) 144636

Contents lists available at ScienceDirect

Journal of Molecular Structure

journal homepage: www.elsevier.com/locate/molstr

Novel chromone–hydrazone conjugates: Synthesis, *in silico* evaluation and cytotoxic assessment against hormone dependent breast cancer cell lines

Akrati Sant [a], Kavya K.M [b], Shama Parveen [c], Ana Ahtsham [c], Krishnaveni S [b], Monisha Banerjee [c], Sonika Bhatia [a,*]

[a] Department of Chemistry, Isabella Thoburn College, University of Lucknow, 226007, India
[b] Department of Studies in Physics, University of Mysore, Mysuru, India
[c] Molecular and Human Genetics Laboratory, Department of Zoology, University of Lucknow, Lucknow 226007, India

ARTICLE INFO

Keywords:
3-formylchromones
Hydrazones
MCF-7
MDA-MB 231
Estrogen receptors
In-silico

ABSTRACT

Given the structural resemblance of the benzopyran-4-one scaffold to 17β-estradiol, this study focused on the synthesis and evaluation of novel 3-formylchromone hydrazone derivatives as potential estrogen receptor-targeting anticancer agents. The compounds were synthesized via a two-step process using 3-formylchromone as a key intermediate and characterized by ^{1}H-NMR, ^{13}C-NMR, FT-IR, and HRMS spectroscopy. Cytotoxicity was assessed against ER-positive MCF-7 and triple-negative MDA-MB-231 breast cancer cell lines, with HEK293 serving as a non-cancerous control. Within the series, compounds **3j, 3c**, and **3e** exhibited the highest potency against MCF-7 cells, with IC_{50} values of 30 μM, 35 μM, and 37 μM, respectively. In contrast, these compounds showed markedly lower activity against MDA-MB-231 cells and displayed minimal cytotoxicity toward HEK293 cells. In silico pharmacokinetic profiling (SwissADME) confirmed favourable drug-like properties, including high gastrointestinal absorption, Lipinski's rule compliance, and absence of PAINS alerts. Molecular docking indicated that compounds **3j** and **3e** aligned closely within the canonical 17β-estradiol binding pocket of estrogen receptor alpha (ERα), exhibiting significant overlap with the native ligand. These findings were further substantiated by molecular dynamics simulations, which confirmed the stability of the ligand–receptor interactions. DFT calculations revealed a low HOMO–LUMO energy gap for compound **3j** (3.69 eV), indicating high reactivity and optimal electrostatic potential. Structure–activity relationship (SAR) analysis highlighted the role of electron-donating substituents in enhancing anticancer activity. Collectively, compounds **3j** and **3e** emerged as the most promising leads for further development as a targeted therapy for hormone-dependent breast cancer, with **3j** being more potent.

1. Introduction

Cancer remains a major global health challenge, responsible for nearly 10 million deaths annually, with breast cancer being one of the most prevalent and life-threatening malignancies among women [1]. Despite advances in chemotherapy, radiotherapy, and immunotherapy, the demand for safer and more selective treatments persists. This has directed attention towards alternative approaches that complement conventional therapies. One such approach is chemoprevention, which involves the proactive use of natural, synthetic, or biological agents to reverse, suppress, or delay the process of carcinogenesis. Among various bioactive scaffolds explored for anticancer activity, chromone and hydrazone derivatives stand out for their structural diversity and pharmacological promise. Hydrazones, characterised by the presence of an azomethine functional group, have been extensively investigated for their various pharmacological activities, including antimicrobial, antimycobacterial, antidepressant, anti-inflammatory, analgesic, antioxidant, and anticancer properties [2–6]. Notable hydrazone-based compounds have exhibited significant antiproliferative activity, often mediated through mechanisms such as metal ion chelation, inhibition of kinases, generation of reactive oxygen species, and disruption of mitochondrial membrane potential [3,7–10]. Their selective toxicity against tumour cells is linked to altered redox metabolism in cancers such as breast, leukaemia and neuroblastoma [7,11–13]. Similarly, chromones, naturally abundant in plants and dietary sources, exhibit diverse anticancer effects, including cytotoxicity, immunomodulation,

* Corresponding author.
E-mail address: sonikaitc2@gmail.com (S. Bhatia).

https://doi.org/10.1016/j.molstruc.2025.144636
Received 2 July 2025; Received in revised form 13 September 2025; Accepted 2 November 2025
Available online 3 November 2025
0022-2860/© 2025 Elsevier B.V. All rights are reserved, including those for text and data mining, AI training, and similar technologies.

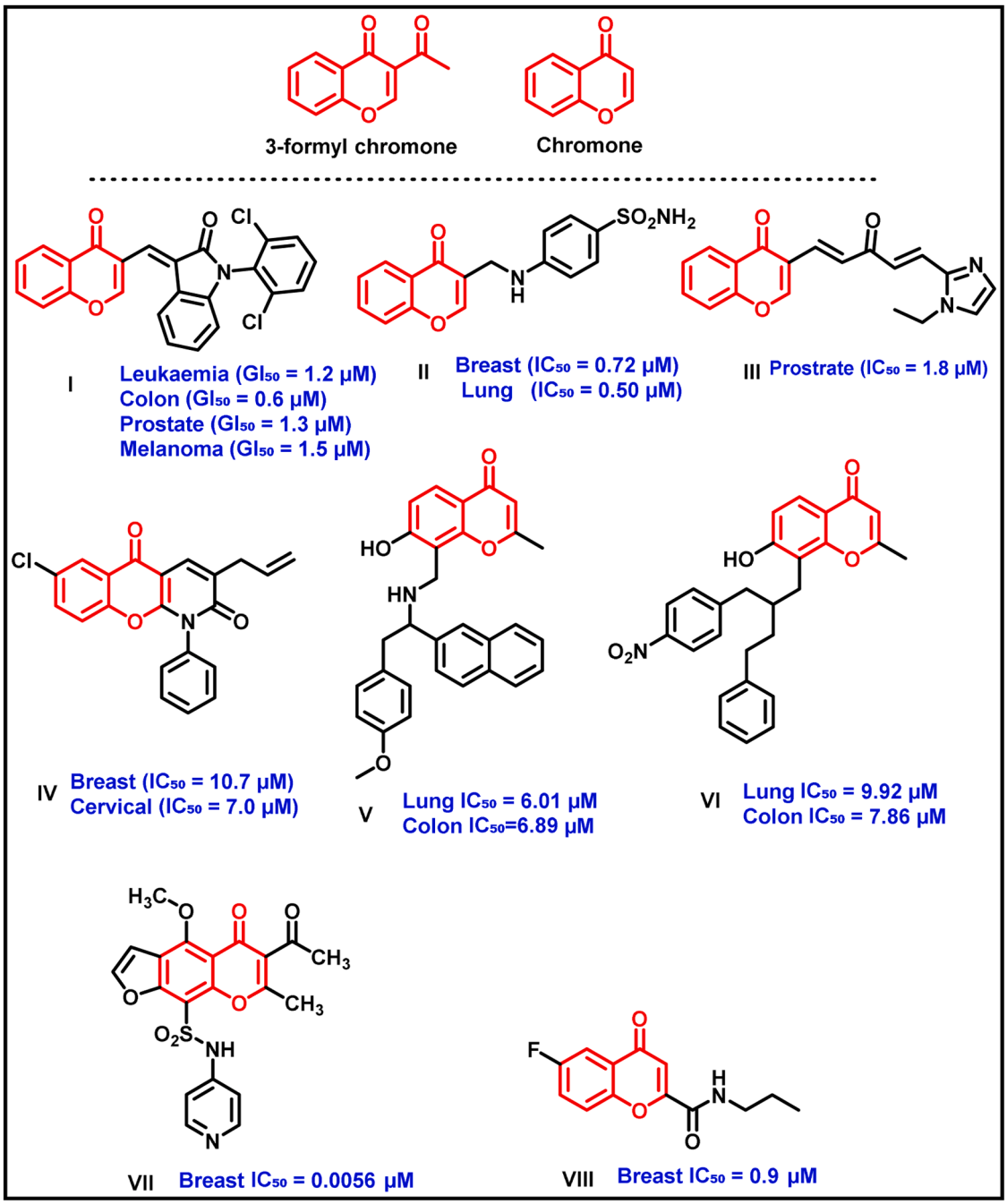

Fig. 1. Representative chromone derivatives with demonstrated anticancer potential.

anti-angiogenic activity, and metastasis inhibition, making them attractive scaffolds for the development of novel therapeutic agents [8,10,14–18].

Compound (**I**) has shown significant growth-inhibitory effects, with reported GI_{50} values of 1.2 μM for leukaemia, 0.6 μM for colon, 1.3 μM for prostate, and 1.5 μM for melanoma cell lines [19]. In particular, compound (**II**) demonstrated apoptosis-inducing activity, showing potent effects against the MCF-7 breast cancer (IC_{50} = 0.72 μM) and A549 lung cancer (IC_{50} = 0.50 μM) cell lines [20]. These derivatives also exhibited selective inhibition of tumour-associated carbonic anhydrase isoforms, suggesting a role in suppressing tumour progression. Furthermore, imidazole (**III**) and compound (**IV**) derivatives have demonstrated promising antiproliferative activity against prostate, breast and cervical cancer cell lines, respectively [21]. Lavendustin analogues also displayed notable efficacy, with compounds (**V**) and (**VI**) achieving IC_{50} values of 6.01 and 9.92 μM against A549 cells, and 6.89 and 7.86 μM against HCT-15 colon cancer cells [21,22]. Compounds (**VII**) and (**VIII**) have demonstrated potent in vitro cytotoxic activity against the MCF-7 breast cancer cell line, with IC_{50} values of 0.0056 ± 0.0027 μM and 0.9 μM, respectively, while exhibiting minimal toxicity toward normal cells [21] (Fig.1). The clinical relevance of chromone-based molecules is further supported by their presence in marketed therapeutic agents such as nedocromil, diosmin, cromolyn, and flavoxate, underscoring their established pharmacological potential. Among various chromone derivatives, 3-formylchromones have attracted particular interest as versatile precursors for the synthesis of Schiff bases [10,23,24]. This is primarily due to their electrophilic C-2 position and the presence of a conjugated keto group at the C-3 position, which makes them ideal candidates for applications in medicinal chemistry [23].

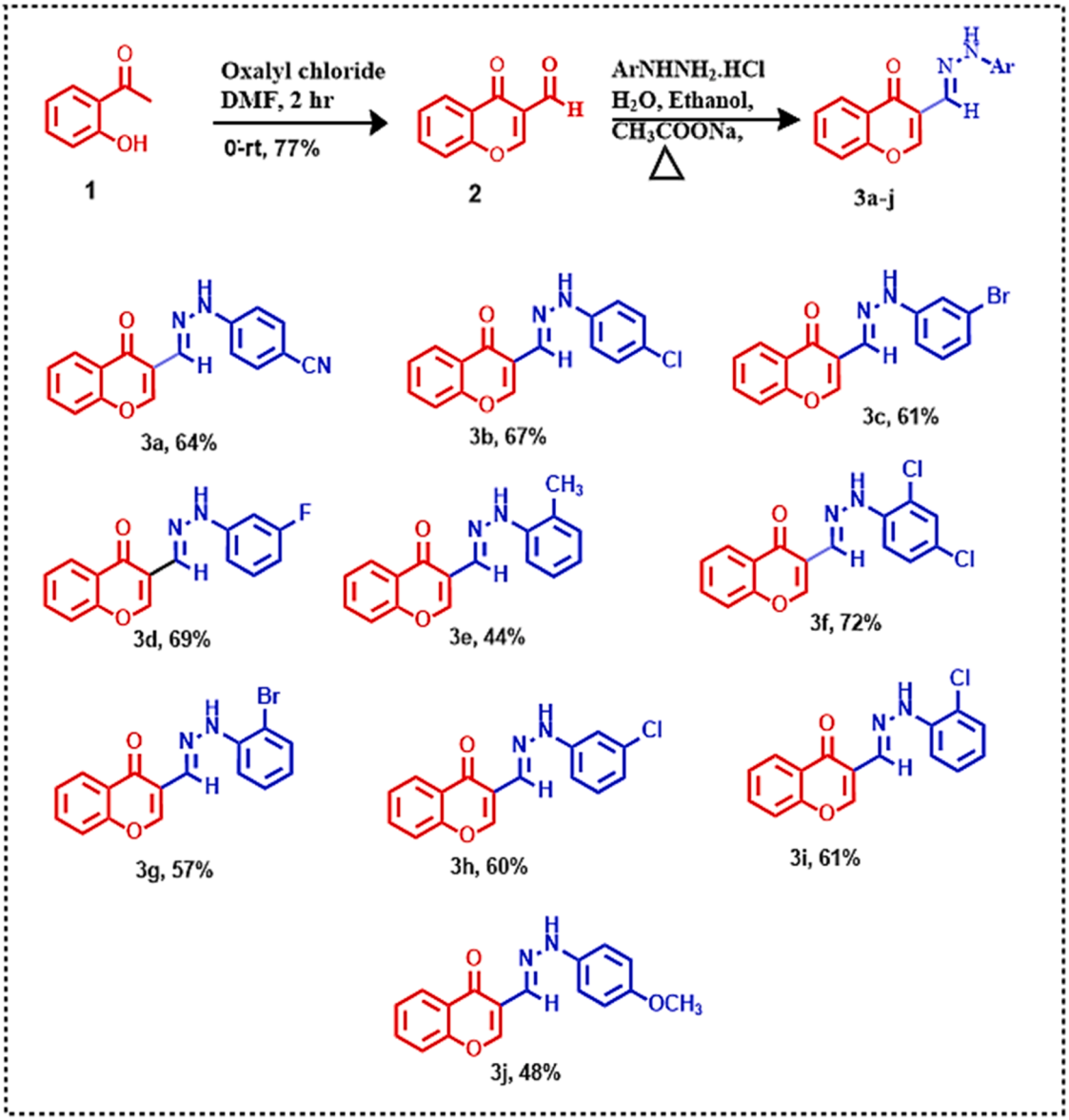

Scheme 1. Synthetic route to the synthesis of 2 followed by 3a-j.

Hydrazone derivatives of 3-formylchromone, obtained through condensation with nitrogen nucleophiles, combine the pharmacophoric features of both hydrazones and chromones. These conjugates exhibit favourable lipophilicity, enabling efficient cellular permeability, and have been explored for diverse biological activities, including kinase inhibition, anticancer, antimicrobial, and anti-inflammatory effects [17, 23].By leveraging the synergistic therapeutic potential of both scaffolds, and considering the structural similarity of the benzopyran-4-one nucleus to 17β-estradiol, such derivatives hold promise as selective estrogen receptor modulators (SERMs). Accordingly, the present study aims to design, synthesize, and evaluate novel 3-formylchromone-derived hydrazones as potential anticancer agents, with an emphasis on their role as SERMs to achieve improved potency and efficacy in breast cancer therapy.

2. Experimental section

2.1. Material and methods

2.1.1. Chemistry

All reagents used for the synthesis and purification of the desired compounds were procured from commercial suppliers and used without further modification. Commercially available solvents, including ethanol, ethyl acetate, sodium bicarbonate and hexane (Rankem, India) and Dimethyl formamide, 2′-hydroxyacetophenone, oxalyl chloride and substituted phenyl hydrazine hydrochlorides (Qualigens >99 %), were utilised in the process. The purity of the synthesised compounds was assessed by thin-layer chromatography (TLC) using silica gel F254 aluminium sheets and further purified by silica gel (60–120 mesh) column chromatography. Spectroscopic characterisation was conducted using various techniques.^{1}H NMR (500/400 MHz) and ^{13}C NMR spectra were recorded on a Bruker Avance III 500 MHz spectrometer. Mass spectra were obtained using a Waters Alliance e2695 HPLC-TQD mass spectrometer (ESI-HRMS/APCI-MS). FT-IR spectra were recorded using the KBr pellet method on a Shimadzu IR Affinity-1S spectrometer,

covering the range of 4000–400 cm^{-1}.

2.1.2. Synthesis

2.1.2.1. General procedure for synthesis of 3-formyl chromone (2). The synthesis began with the preparation of the 3-formylchromone intermediate, following a literature-reported procedure (Scheme 1) [25]. In a round-bottom flask, 2′-hydroxyacetophenone (0.88 mmol) was mixed with dimethylformamide (DMF, 1.7 mmol). Under continuous stirring at 0 °C, oxalyl chloride (0.88 mmol) was added dropwise. The reaction progress was monitored using thin-layer chromatography (TLC) with a mobile phase of 0.5 % methanol in chloroform. Upon completion, the reaction mixture was quenched and neutralised using ice and sodium bicarbonate. The resulting solid precipitate was washed sequentially with water, followed by 15 % ethyl acetate in hexane. The final product was vacuum-dried, characterised by mass spectrometry and NMR and collected for subsequent steps.

2.1.2.2. General synthesis procedure for chroman hydrazone derivatives (3a-j). Substituted phenyl hydrazine hydrochlorides (0.4 mmol) were dissolved in 5–6 mL of water and basified with sodium acetate (1.1 mmol), as outlined in Scheme 1. The mixture was gently heated in a water bath for 5 minutes. Subsequently, an ethanolic solution of 3-formylchromone (**2**) (0.2 mmol) was added, and the reaction was further heated for 5–10 minutes for all derivatives, except for compounds **3e** and **3j**, which required an extended reaction time of 30–60 minutes. The progress of the reaction was monitored using thin-layer chromatography (TLC) with a mobile phase consisting of 0.5 % methanol in chloroform. Upon completion, the reaction mixture was allowed to cool, and the resulting precipitate was collected by vacuum filtration. The crude product was further purified by column chromatography using a chloroform–methanol (9.5:0.5) solvent system.

2.1.1.3. Characterisation data. **4-oxo-4*H*-chromene-3-carbaldehyde (2):** White solid Powder, M.P- 150-156°C, R_f = 0.3, **^{1}H-NMR (400 MHz, $CDCl_3$)** δ = 10.38 (s, 1H), 8.61 (s, 1H), 8.30 (dd, 1H), 7.74 (s, 1H), 7.52-7.47 (d, 2H). **^{13}C-NMR ($CDCl_3$)-** 188.7, 176.07, 160.72, 156.29, 134.92, 126.73, 126.26, 125.41, 120.42, 118.71. **ESI-MS-M/Z-** Calculated-174.0, found [M+H$^+$] = 175.0.

4-(2-((4-oxo-4*H*-chromen-3-yl) methylene) hydrazonoyl) benzonitrile (3a): Yellow solid powder, M.P- 202-210°C, R_f = 0.4, **^{1}H-NMR (400 MHz, $CDCl_3$)** δ = 8.58 (s, 1H), 8.27 (s, 1H), 8.04 (s, 1H), 8.01 (s, 1H), 7.71 (s, 1H), 7.54 (d, 1H), 7.52 (d, 2H), 7.45 (d, 2H), 7.10 (dd, 1H), 7.08 (dd, 1H). **^{13}C-NMR ($CDCl_3$)-** 176.45, 158.2, 152.83, 138.95, 135.8, 132.46, 129.03, 127, 126.2, 123.8 120.38, 117.11, 116.63. **ESI-HRMS-M/Z-** Calculated- 290.0924, found [M+H$^+$] = 290.0922. **FT-IR KBr (cm^{-1}):** 3252 (=CH), 2933 (NH), 2221 (CN), 1613 (CO), 1551 (C=N), 1286 (C-O), 1144 (N-N).

3-((2-(4-chlorophenyl) hydrazinylidene) methyl)-4*H*-chromen-4-one (3b): Yellow powder, M.P- 203-204°C, R_f = 0.6, **^{1}H-NMR (400 MHz, $CDCl_3$)** δ = 8.55 (s, 1H), 8.26 (s, 1H), 7.96 (s, 1H), 7.78 (s, 1H), 7.68 (s, 1H), 7.54 (d, 1H), 7.4 (d, 2H), 7.23 (d, 2H), 7.1 (d, 2H), 7.08 (dd, 1H) **^{13}C-NMR ($CDCl_3$)-** 176.06, 156.26, 151.84, 143.67, 133.83, 129.02, 128.99, 125.80, 125.44, 123.88, 120.04, 118.43, 113.65. **ESI-HRMS-M/Z-** Calculated- 299.0509, found [M+H$^+$] = 299.0578. **FT-IR KBr (cm^{-1}):** 3282 (=CH), 2965 (NH), 1629 (CO), 1473 (C=N), 1286 (C-O), 1091 (N-N).

3-((2-(3-bromophenyl) hydrazinylidene) methyl)-4*H*-chromen-4-one (3c): Yellowish green, M.P- 202-205°C, R_f = 0.8, **^{1}H-NMR (400 MHz, $CDCl_3$)** δ = 8.53 (s, 1H), 8.27 (s, 2H), 8.21 (s, 1H), 8.06 (s, 1H), 7.65 (s, 1H), 7.46 (s, 1H), 7.38 (d, 1H), 7.23 (d, 1H), 7.16 (d, 1H), 6.75 (dd, 1H). **^{13}C-NMR ($CDCl_3$)-** 175.96, 156.-34, 152.38, 140.41, 133.96, 131.42, 129.28, 127.92, 126.05, 125.62, 120.32, 118.45, 117.13, 114.03. **ESI-HRMS-M/Z-** Calculated- 343.0004, found [M+H$^+$] = 343.0077. **FT-IR KBr (cm^{-1}):** 3284 (=CH), 2920 (NH), 1637 (CO), 1589 (C=N), 1247 (C-O), 1145 (N-N).

3-((2-(3-fluorophenyl) hydrazinylidene) methyl)-4*H*-chromen-4-one (3d): Yellow powder, M.P- 199-200°C, R_f = 0.7, **^{1}H-NMR (400 MHz, $CDCl_3$)** δ = 8.66 (s, 1H), 8.53 (s, 1H), 8.22 (s, 1H), 8.20 (s, 1H), 7.98 (d, 1H), 7.65 (d, 1H), 7.48 (d, 1H), 7.14 (d, 1H), 6.86 (dd, 1H), 6.72 (dd, 1H), 6.48 (dd, 1H) . **^{13}C-NMR ($CDCl_3$)-** 176.45, 158.2, 152.83, 138.95, 135.8, 132.46, 129.03, 127, 126.2, 123.8 120.38, 117.11, 116.63. **ESI-HRMS-M/Z-** Calculated- 283.0805, found [M+H$^+$] = 283.0878. **FT-IR KBr (cm^{-1}):** 3410 (=CH), 2929 (NH), 1591 (CO), 1463 (C=N), 1242 (C-O), 1128 (N-N).

3-((2-(o-tolyl) hydrazinylidene) methyl)-4*H*-chromen-4-one (3e): Brown solid, M.P- 205-210°C, R_f = 0.3, **^{1}H-NMR (400 MHz, $CDCl_3$)** δ = 8.41 (s, 1H), 8.3 (s, 1H), 8.03 (s, 1H), 7.96(s, 1H), 7.78 (s, 1H), 7.5 (d, 1H), 7.4 (d, 2H), 7.3 (d, 2H), 7.24(d, 2H), 7.08 (dd, 1H), 2.9 (s, 3H). **^{13}C-NMR ($CDCl_3$)-** 173, 158.2, 152.83, 138.95, 135.8, 132.46, 129.03, 127, 126.2, 123.8 120.38, 117.11, 116.63. **ESI-HRMS-M/Z-** Calculated- 279.1055, found [M+H$^+$] = 279.1119, **FT-IR KBr (cm^{-1}):** 3429 (=CH), 2935 (NH), 1606 (CO), 1502 (C=N), 1280 (C-O), 1139 (N-N).

3-((2-(2,4-dichlorophenyl) hydrazinylidene) methyl)-4*H*-chromen-4-one (3f): Yellow solid, M.P- 205-210°C, R_f = 0.6, **^{1}H-NMR (400 MHz, DMSO)** δ = 10.2 (s, 1H), 8.88 (s, 1H), 8.43 (s, 1H), 8.13(s, 1H), 7.83 (s, 1H), 7.7 (d, 1H), 7.6 (d, 1H), 7.55 (d, 1H), 7.45(d, 1H), 7.23 (dd, 1H) . **^{13}C-NMR (DMSO)-** 175.45, 156.22, 153.83, 140.95, 134.87, 133.46, 129.03, 128.38, 126.30, 125.68, 123.80, 122.87, 119.76, 119.12, 117.14, 115.8. **ESI-HRMS-M/Z-** Calculated- 333.0119, found [M+H$^+$] = 333.0180. **FT-IR KBr (cm^{-1}):** 3271 (=CH), 2744 (NH), 1633 (CO), 1514 (C=N), 1298 (C-O), 1120 (N-N).

3-((2-(2-bromophenyl) hydrazinylidene) methyl)-4*H*-chromen-4-one (3g): Yellowish green, M.P- 201-203°C, R_f = 0.8, **^{1}H-NMR (400 MHz, $CDCl_3$)** δ = 8.55 (s, 1H), 8.25 (s, 1H), 8.23 (s, 1H), 8.20 (s, 1H), 8.08 (s, 1H), 7.67 (d, 1H), 7.65 (d, 2H), 7.49 (d, 1H), 7.42 (d, 1H), 7.40 (dd, 1H), 6.72(s, 1H) **^{13}C-NMR ($CDCl_3$)-** 176.45, 158.2, 152.83, 138.95, 135.8, 132.46, 129.03, 127, 126.2, 123.8 120.38, 117.11, 116.63. **ESI-HRMS-M/Z-** Calculated- 343.0004, found [M+H$^+$] = 343.0077 **FT-IR KBr (cm^{-1}):** 3257 (=CH), 2929 (NH), 1629 (CO), 1508 (C=N), 1203(C-O), 1039 (N-N).

3-((2-(3-chlorophenyl) hydrazinylidene) methyl)-4*H*-chromen-4-one (3h): Yellow powder, M.P- 205-206°C, R_f = 0.5, **^{1}H-NMR (400 MHz, $CDCl_3$)** δ = 8.55 (s, 1H), 8.21 (s, 1H), 7.97 (s, 1H), 7.66(s, 1H), 7.49 (s, 1H), 7.43 (d, 1H), 7.28 (d, 2H), 7.05 (d, 2H), 6.91 (dd, 1H), **^{13}C-NMR ($CDCl_3$)-** 176.45, 158.2, 152.83, 138.95, 135.8, 132.46, 129.03, 127, 126.2, 123.8 120.38, 117.11, 116.63. **ESI-HRMS-M/Z-** Calculated-299.0509, found [M+H$^+$] = 299.0578. **FT-IR KBr (cm^{-1}):** 3276(=CH), 2914 (NH), 1622 (CO), 1471 (C=N), 1227 (C-O), 1101 (N-N).

3-((2-(2-chlorophenyl) hydrazinylidene) methyl)-4*H*-chromen-4-one (3i): Yellow powder, M.P- 201-206°C, R_f = 0.4, **^{1}H-NMR (400 MHz, $CDCl_3$)** δ = 8.93 (s, 1H), 8.52 (s, 1H), 8.17 (s, 1H), 7.96(s, 1H), 7.63 (s, 1H), 7.46 (d, 1H), 7.37 (d, 2H), 7.09 (d, 2H), 6.84 (d, 2H), 6.70 (dd, 1H), **^{13}C-NMR ($CDCl_3$)-** 176.45, 158.2, 152.83, 138.95, 135.8, 132.46, 129.03, 127, 126.2, 123.8 120.38, 117.11, 116.63. **ESI-HRMS-M/Z-** Calculated- 299.0509, found [M+H$^+$] = 299.0578. **FT-IR KBr (cm^{-1}):** 3280 (=CH), 3068 (NH), 1618 (CO), 1504 (C=N), 1228 (C-O), 1045 (N-N).

3-((2-(4-methoxyphenyl) hydrazinylidene) methyl)-4*H*-chromen-4-one (3j): Brown solid, M.P- 205-210°C, R_f = 0.3, **^{1}H-NMR (400 MHz, $CDCl_3$)** δ = 11.07 (s, 1H), 8.92 (s, 1H), 8.10 (s, 1H), 7.83 (dd, 1H), 7.80 (dd, 1H), 7.45 (s, 1H), 7.05-7.02 (s, 2H), 6.95 (d, 1H), 3.76 (s, 3H). **^{13}C-NMR ($CDCl_3$)-** 190.76, 159.18, 159.02, 142.69, 134.85, 132.86, 132.96, 131.88, 131.25, 124.04, 123.88, 121.48, 119.86, 117.86, 115.17, 56.04. **ESI-HRMS-M/Z-** Calculated- 295.1073, found [M+H$^+$] = 295.1089, **FT-IR KBr (cm^{-1}):** 3419 (=CH), 2946 (NH), 1612 (CO), 1508 (C=N), 1259 (C-O), 1091 (N-N).

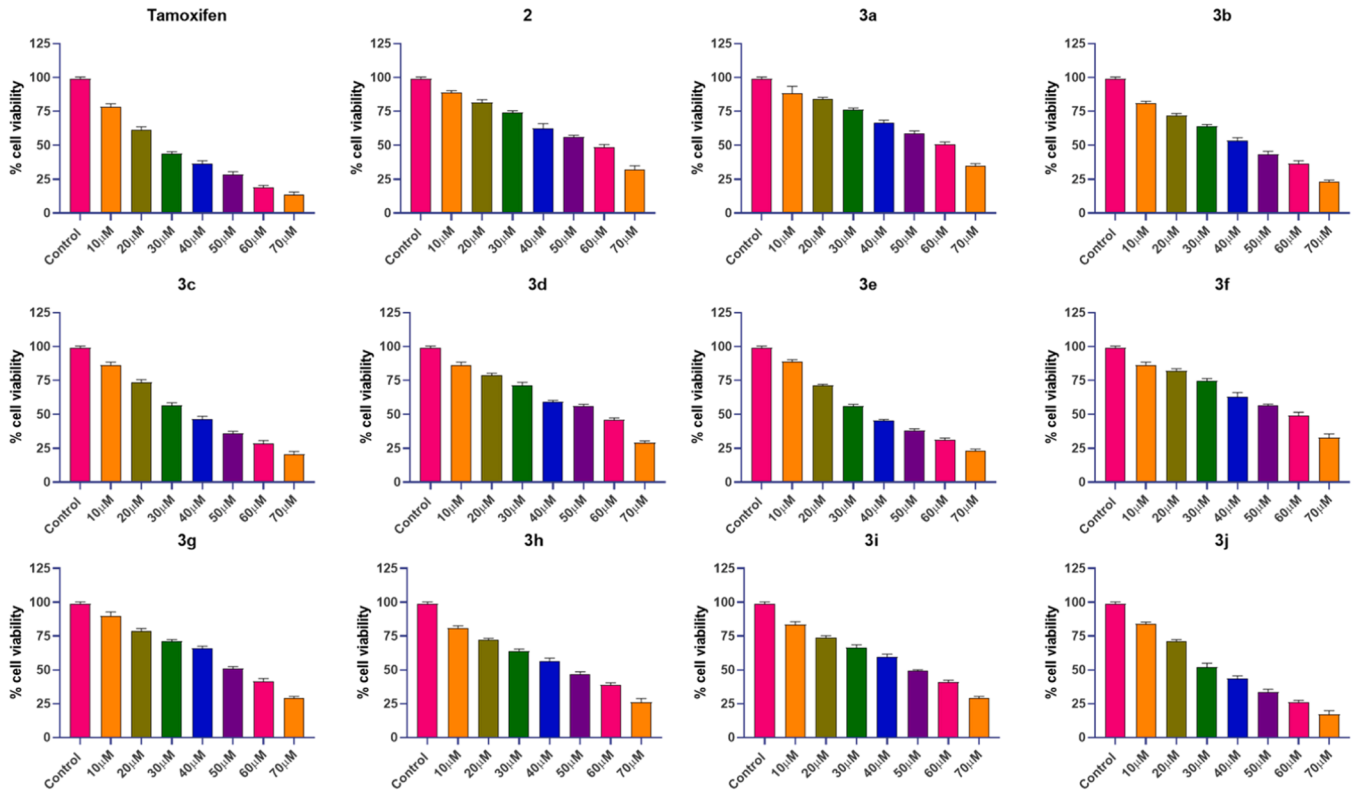

Fig. 2. Cell viability assay of MCF-7 breast cancer cells treated with Tamoxifen and compounds 2 and 3a–j at varying concentrations. Data are expressed as mean ± standard deviation (SD) from three independent experiments (n = 3).

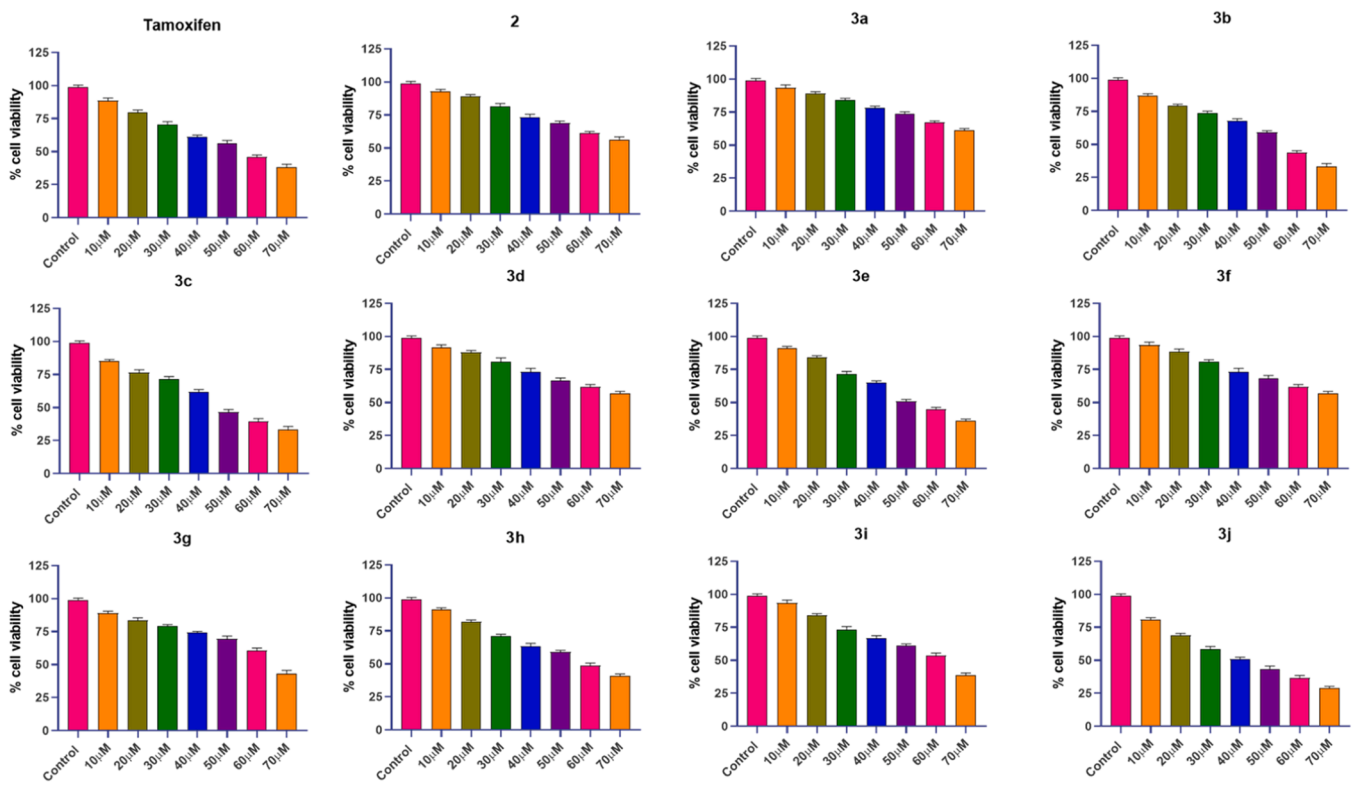

Fig. 3. Cell viability assay of MDA-MB-231 treated with Tamoxifen and compounds 2 and 3a–j at varying concentrations. Data are expressed as mean ± standard deviation (SD) from three independent experiments (n = 3).

Table 1
IC_{50} Value (μM) on hormone-dependent & triple negative breast cancer cell lines.

Compounds/Code	IC_{50} Value (μM)	
	MCF-7	MDA-MB-231
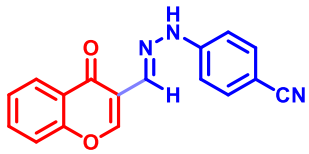	**60**	81
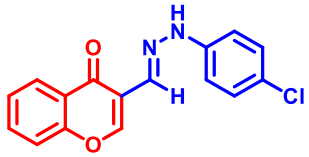	**42**	56
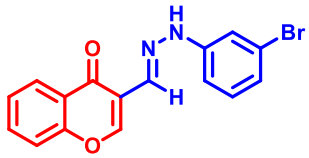	**35**	47
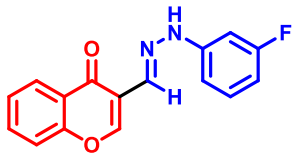	**55**	74
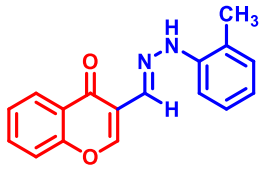	**37**	50
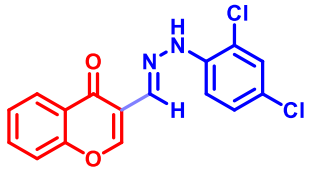	**57**	77
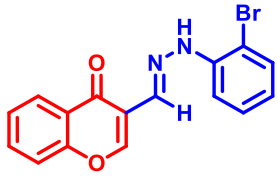	**50**	67
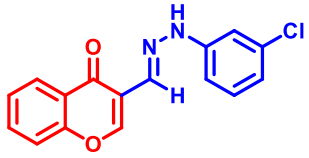	**45**	60
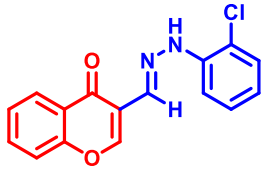	**47**	63

Table 1 (*continued*)

Compounds/Code	IC_{50} Value (μM)	
	MCF-7	MDA-MB-231
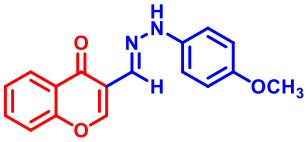	**30**	40
2 (Intermediate)	**57**	**77**
Tamoxifen (Control)	**27**	**57**

2.1.2. Biology

2.1.2.1. Materials and Methods

2.1.2.1.1. Cell Culture. Human breast cancer MCF-7, MDA-MB-231 (Triple negative breast cancer) cells and human epithelial cell line HEK293 (non-tumorous) were used in the current study. The cell line was procured from the National Centre for Cell Sciences in Pune, India. The cells were maintained in DMEM (Dulbecco's Modified Eagle Medium) medium supplemented with 10 % FBS (Fetal Bovine Serum) and 1 % antibiotic-antimycotic solution and placed in CO_2 incubator at 37°C with 5 % CO_2.

2.1.2.1.2. MTT assay. The MTT assay is based on the ability of the cells to convert the yellow 3-(4,5-dimethylthiazol-2-yl)-2,5-diphenyltetrazolium bromide salt (MTT) into purple formazan crystals by the mitochondrial dehydrogenase enzyme. Integrity and activity of mitochondria are interpreted as an indicator of cell viability [26]. All the cell lines were seeded (1×10^4 in each well) in a 96 well plate and incubated for 24 h. Thereafter, the cells were treated with different concentrations (10-70μM) of **Tamoxifen, 2** and **3a-j** for 24 h. After 24 h of exposure, 10 μL of MTT solution (5 mg/mL) in PBS (phosphate buffered saline) was added to each well and incubated in a CO_2 incubator for 3 h. The culture medium was discarded after incubation, and 100 μL of DMSO (Dimethyl sulfoxide) was added to dissolve crystals. After 15 min incubation, OD (optical density) was measured at 540 nm using a microplate reader (BioTek, Epoch 2, USA.

2.1.3. In silico studies

2.1.3.1. Swiss ADME evaluation. The physical and pharmacological characteristics of the synthesized compounds were predicted using the SwissADME software [27]. Key physicochemical properties analysed included the number of hydrogen bond donors and acceptors, topological polar surface area (TPSA), and molar refractivity. Additionally, pharmacokinetic parameters such as skin permeability (log Kp), cytochrome P enzyme inhibition, P-glycoprotein (P-gp) substrate status, blood-brain barrier (BBB) permeability, gastrointestinal (GI) absorption, and lipophilicity (log P o/w) were evaluated. These factors are crucial in predicting drug absorption and distribution within the body. Drug-likeness was assessed based on Lipinski's rule of five. The following established formula was used to determine the compound's percentage absorption (% Abs) [28].

$$\% \text{ Abs} = 109\text{-}0.345 \times \text{TPSA}$$

2.1.3.2. Molecular docking. The structures of the synthesized compounds (**3a-j**) were drawn using ChemDraw software (RRID: SCR_016768). Then these compounds were subjected to molecular docking studies with the estrogen receptor alpha (ERα) to investigate the mode of action underlying the experimentally observed IC_{50} values. The crystal structure of ERα was retrieved from the RCSB Protein Data Bank (PDB ID: 3ERT) [29,30]. The retrieved ERα protein imported into AutoDock 4.2.6 [31,32] and prepared for docking by adding polar hydrogen atoms and assigning Kollman charges (2.185). Similarly, the compounds (**3a-j**) were prepared by introducing polar hydrogen atoms

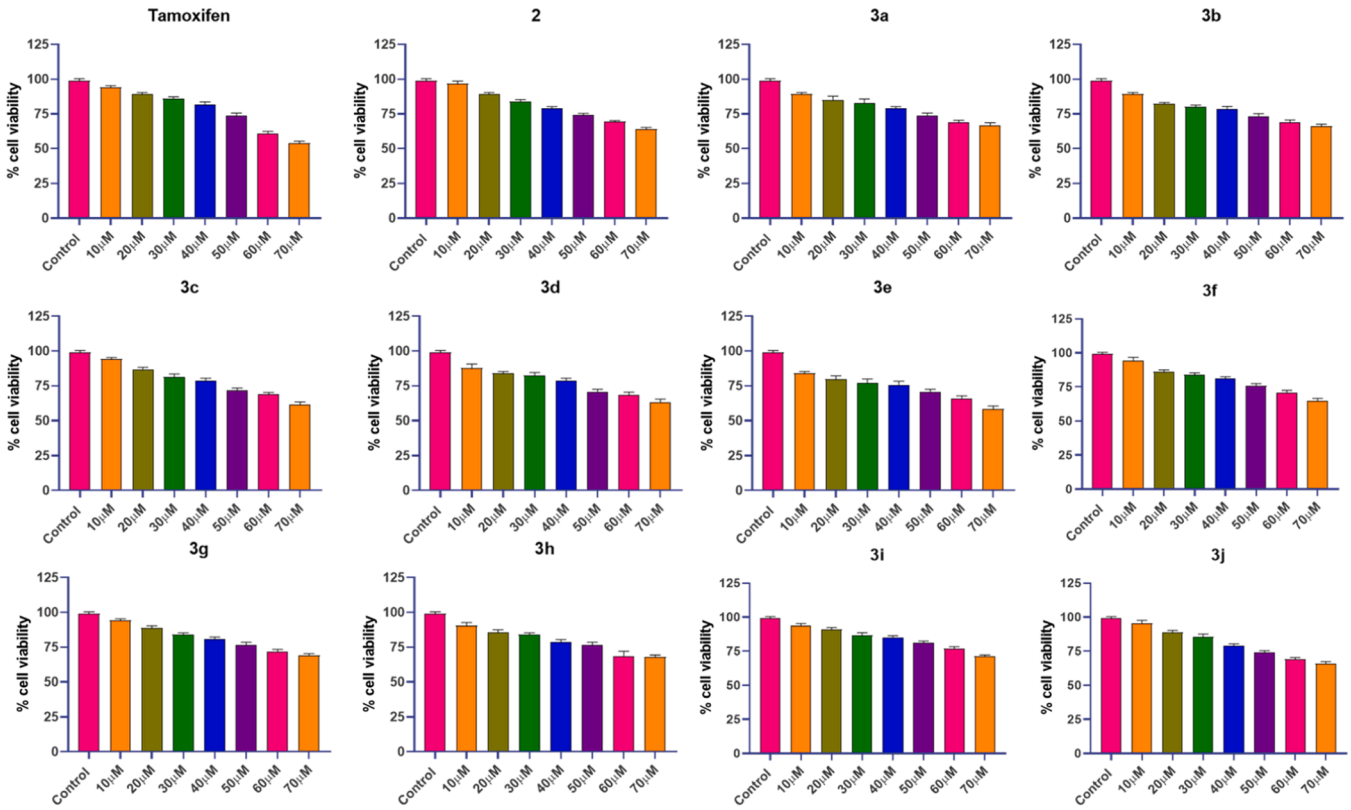

Fig. 4. Cell viability assay of HEK293 treated with Tamoxifen and compounds 2 and 3a–j at varying concentrations. Data are expressed as mean ± standard deviation (SD) from three independent experiments (n = 3).

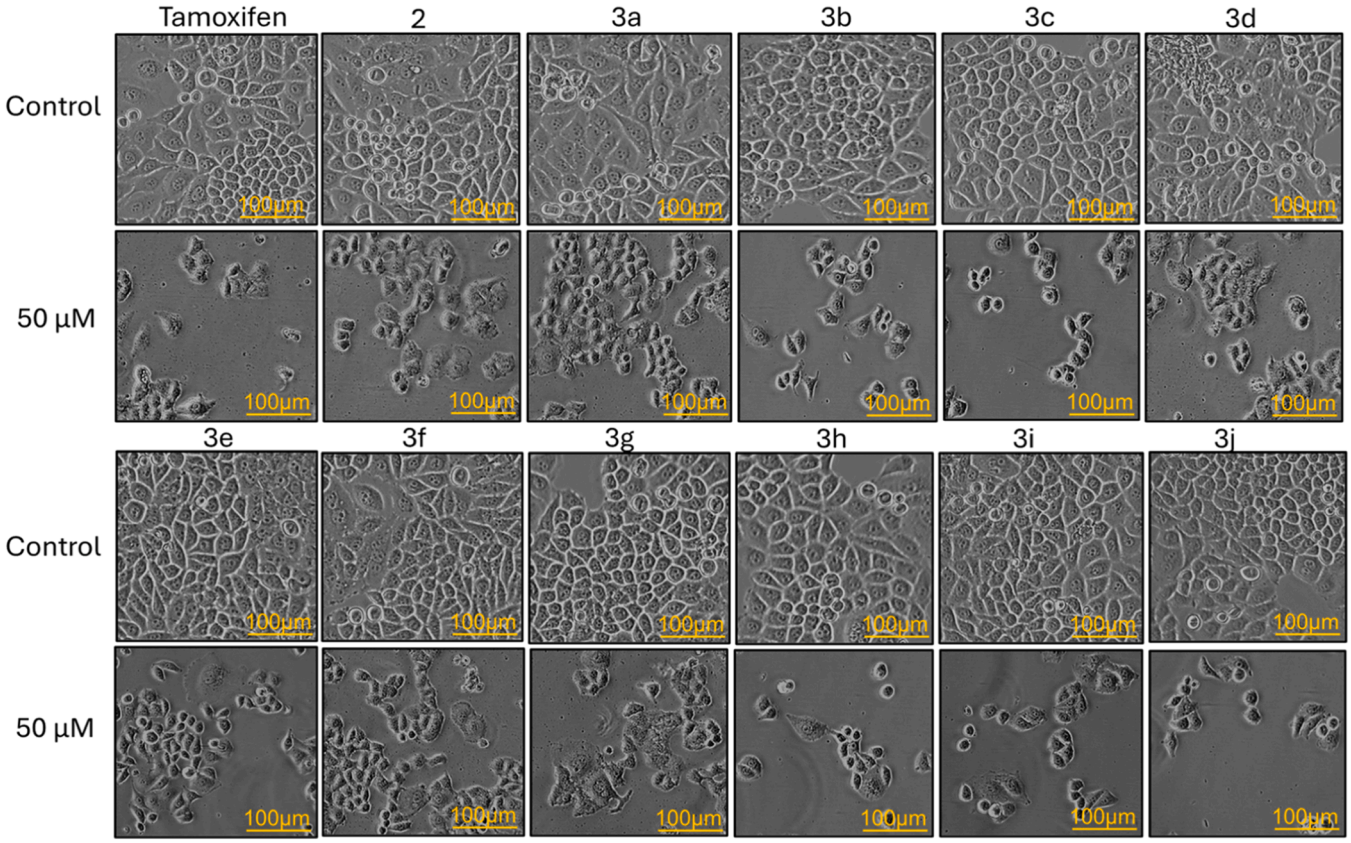

Fig. 5. Representative morphological images of MCF-7 cells treated with Tamoxifen and compounds 2 and 3a–j at a concentration of 50 μM.

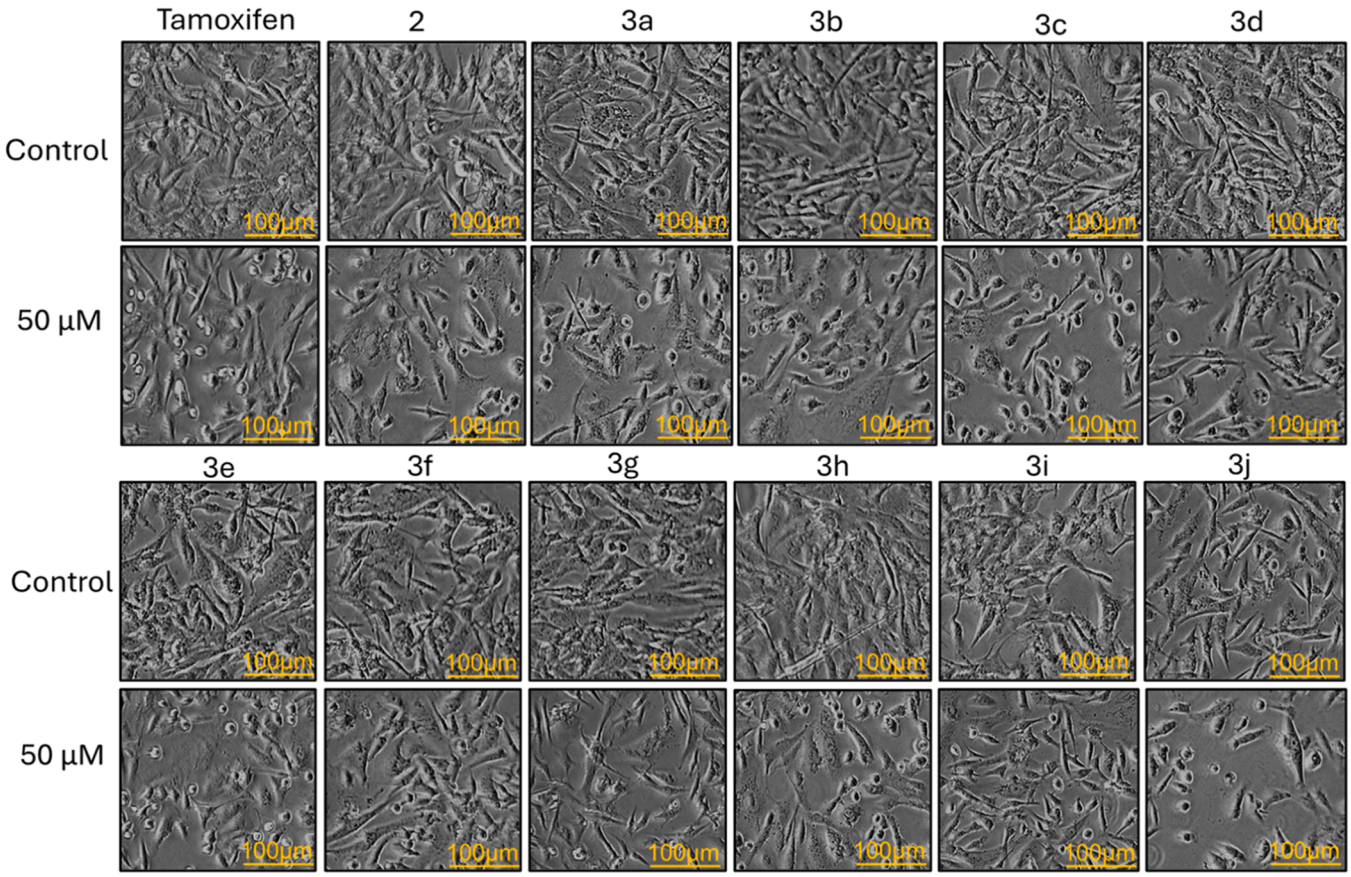

Fig. 6. Representative morphological images of MDA-MB-231 cells treated with Tamoxifen and compounds 2 and 3a–j at a concentration of 50 µM.

Table 2
ADME properties data of compound **3 a-j**.

Properties	Compounds									
	3a	3b	3c	3d	3e	3f	3g	3h	3i	3j
PHARMACOKINETICS										
BBB Permeant	Yes	Yes	Yes	Yes	Yes	Yes	Yes	Yes	Yes	Yes
GI absorption	High	High	High	High	High	High	High	High	High	High
P-gp substrate	No	No	No	No	No	No	No	No	No	No
CYP1A2 inhibitor	Yes	Yes	Yes	Yes	Yes	Yes	Yes	Yes	Yes	Yes
CYP2C19 inhibitor	Yes	Yes	Yes	Yes	Yes	Yes	Yes	Yes	Yes	Yes
CYP2C9 inhibitor	Yes	Yes	Yes	Yes	Yes	Yes	Yes	Yes	Yes	Yes
CYP2D6 inhibitor	No	No	No	No	Yes	No	No	No	No	Yes
CYP3A4 inhibitor	Yes	No	No	No	Yes	No	No	No	No	Yes
DRUG LIKENESS										
Lipinski rule	Yes	Yes	Yes	Yes	Yes	Yes	Yes	Yes	Yes	Yes
Ghose	Yes	Yes	Yes	Yes	Yes	Yes	Yes	Yes	Yes	Yes
Veber	Yes	Yes	Yes	Yes	Yes	Yes	Yes	Yes	Yes	Yes
Egan	Yes	Yes	Yes	Yes	Yes	Yes	Yes	Yes	Yes	Yes
Muegge	Yes	Yes	Yes	Yes	Yes	Yes	Yes	Yes	Yes	Yes
Bioavailability Score	0.55	0.55	0.55	0.55	0.55	0.55	0.5	0.55	0.55	0.55
MEDICINAL CHEMISTRY										
PAINS	0 alert	0 alert	0 alert	0 alert	0 alert	0 alert	0 alert	0 alert	0 alert	0 alert
Brenk	1 alert	1 alert	1 alert	1 alert	1 alert	1 alert	1 alert	1 alert	1 alert	1 alert
Lead likeness	Yes	No	No	Yes	No	No	No	No	No	Yes
Synthetic accessibility	3.23	3.06	3.11	3.06	3.18	3.12	3.13	3.16	3.08	3.06

and assigning Gasteiger partial charges, with torsional flexibility enabled. Then, a grid box was constructed with dimensions of 126 × 126 × 126 points (centered on x = 22.397, y = 5.643, and z = 21.988) with a grid point spacing of 0.375 Å. Following this, the Lamarckian genetic algorithm was utilized to search for binding positions, with the energy generation limited to 27000 and a population size of 150 individuals, with a maximum of 2500000 energy evaluations permitted. Upon completion, ten conformations of the ligands in complex with the protein were obtained. The analysis of docking results and image rendering was conducted using Chimera and Discovery Studio Biovia software.

2.1.3.3. Molecular dynamics. Molecular dynamics (MD) simulations

Table 3
Physicochemical properties and medicinal chemistry data of compound **3 a-j** calculated using Swiss ADME properties.

Compound	MW	NHBAs	NHBDs	TPSA	%Abs	MR	Log S	Log P
3a	289.29	4	1	78.39	85.17	84.68	-3.92	2.44
3b	298.72	3	1	54.60	59.32	84.97	-4.58	2.76
3c	298.72	3	1	54.60	59.32	84.97	-4.58	2.77
3d	282.27	4	1	54.60	59.32	79.92	-4.14	2.58
3e	278.31	3	1	54.60	59.32	84.93	-4.29	2.84
3f	333.17	3	1	54.60	59.32	89.98	-5.16	3.17
3g	343.17	3	1	54.60	59.32	87.66	-4.89	3.02
3h	343.17	3	1	54.60	59.32	87.66	-4.89	3.48
3i	298.72	3	1	54.60	59.32	84.97	-4.58	2.89
3j	294.30	4	1	63.83	69.35	86.45	-4.04	2.78

Abbreviations: MW = molecular weight (g/mol), NHBAs = number of hydrogen bond acceptors, NHADs = number of hydrogen bond donors, TPSA = Topological polar surface area, % Absorption = Gastro intestinal absorption, MR = Molar refractivity, Log S = logarithmic n-octanol-water partition coefficient, Log P = Logarithm of the partition coefficient.

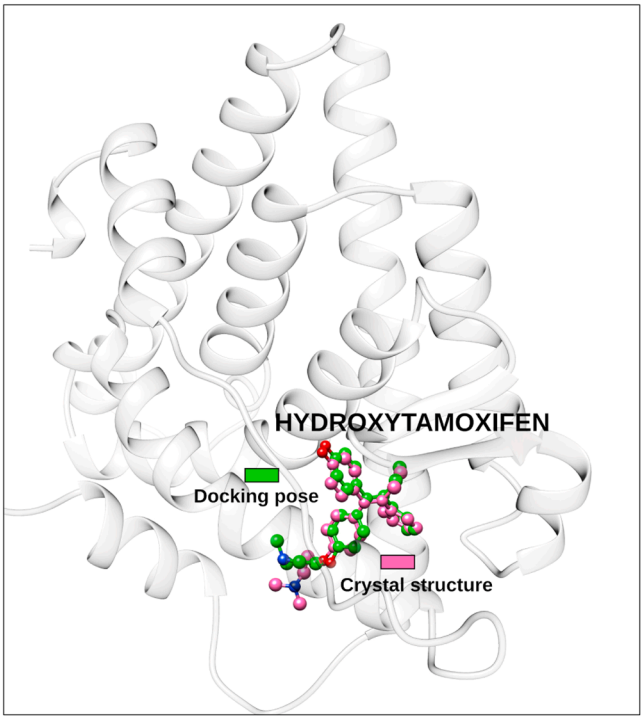

Fig. 7. Comparison of hydroxytamoxifen binding poses: crystal structure (PDB ID: 3ERT, pink) versus docked pose (green). The RMSD between the two conformations is 1.19 Å, validating the docking protocol.

Table 4
Binding energies of the synthesized compounds (**3a-j**) in kcal/mol.

Compounds	ER-α	ER-β	HER-2	PR
3a	-7.63	-7.36	-8.77	-8.94
3b	-7.89	-6.92	-7.87	-8.26
3c	-8.2	-7.45	-8.44	-8.85
3d	-7.62	-7.3	-7.5	-7.97
3e	-7.47	-7.45	-7.92	-8.51
3f	-7.81	-6.88	-8.47	-8.92
3g	–7.8	-7.88	-8.79	-8.89
3h	-7.82	-7.4	-8.18	-8.5
3i	-8.05	-7.65	-8.01	-8.64
3j	-7.29	-8.21	-7.9	-8.57
Tamoxifen	-10.93	-8.32	-8.75	-10.89

were conducted to assess the structural stability and binding energy of the ERα protein with the inhibitor compounds **3c, 3e**, and **3j**. MD simulations for all complexes were performed using GROMACS-24.3 [33–35] package by employing the standard protocols described in the following references [36–39]. Initially, the proteins and compounds were separated from the docked protein PDB file using UCSF Chimera-1.19 [40]. For the separated protein structure, the CHARMM36 force field was used to assign topology parameters [41–44], while the CGenFF server provided topology information for the compounds **3c, 3e**, and **3j** [45,46]. Each protein-compound complex was then centered within a triclinic box, maintaining a 1.2 nm distance between the protein and the box edges to prevent edge effects. The system was then solvated using the TIP3P water model [47,48], and Cl^- and Na^+ ions were introduced to neutralize the system's net charge. Energy minimization was performed to remove steric clashes. Subsequently, NVT equilibration was conducted at 300 K for 1 ns using the V-rescale thermostat [49] for temperature regulation, followed by NPT equilibration at 1 bar pressure for 1 ns using the Parrinello-Rahman barostat [50]. Long-range electrostatic interactions were managed using the Particle Mesh Ewald (PME) method [51,52], and H-bond constraints were applied with the Linear Constraints Solver (LINCS) [53]. Upon equilibration of the systems, 100 ns molecular dynamics (MD) simulations were carried out in the NPT ensemble at 300 K and 1 bar [54], using the V-rescale thermostat and Parrinello-Rahman barostat to maintain both temperature and pressure stability throughout the simulations. The resulting MD simulation trajectories were analyzed for root mean square deviation (RMSD), root mean square fluctuations (RMSF), solvent-accessible surface area (SASA), radius of gyration (Rg), H-bond interaction, and non-bonded interaction energy (comprising electrostatic and van der Waals interactions) between the protein and compounds. These analyses were conducted using GROMACS inbuilt packages. Visualization and image rendering were performed with VMD-1.9.4 (Visual Molecular Dynamics) [55] and UCSF Chimera-1.19 [40,56], while graphs were generated using Gnuplot.

2.1.3.4. Density functional theory. The structures of compounds **3c, 3e**, and **3j** were geometry-optimized using the ORCA 6.0.1 program [57] with the B3LYP functional [58] and the 6-31G basis set [59], without applying any symmetry constraints. For these optimized structures, Frontier Molecular Orbitals (HOMO and LUMO) were generated and visualized using Avogadro software [60], and their corresponding energies were calculated. Following this, electrostatic potential regions of the optimized complexes were generated using the orca vpot module and visualized through illustrations created with UCSF Chimera software [40].

3. Results

3.1. Chemistry

A series of substituted chromone-based hydrazones were synthesized via a two-step reaction sequence. In the first step, 2′-

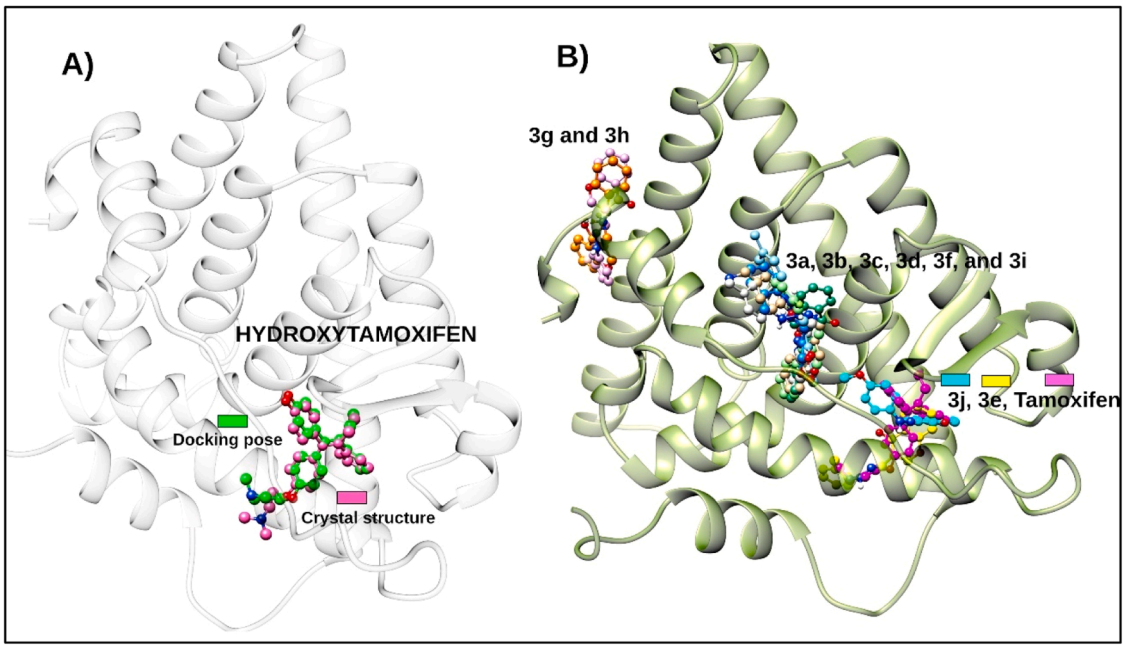

Fig. 8. (**A**) Compounds 3j and 3e bind at the 17β-estradiol site of ERα, overlapping with the native hormone's binding pocket. (**B**) Binding of 3g, 3h, and 3a-f, 3i at an alternate site distinct from the estradiol-binding region.

hydroxyacetophenone (**1**) was reacted with oxalyl chloride and DMF under zero to room temperature conditions to generate 3-formylchromone (**2**). The reaction of the aforementioned reactants proceeds via a Vilsmeier–Haack formylation, introducing a formyl group at the C-3 position of the chromone ring to yield 3-formylchromone (**2**). The resulting intermediate (**2**) was obtained in good yield and used directly in subsequent steps without further purification. In the second step, condensation of the 3-formylchromone (**2**) with various substituted phenyl hydrazines yielded the corresponding hydrazone derivatives (**3a–j**). The aldehyde group of 3-formylchromone (**2**) undergoes a nucleophilic addition–elimination reaction with various phenyl hydrazines, resulting in the formation of a (–CH=N–NH–Ar) hydrazone linkage. This condensation reaction is typically acid/base-catalysed and proceeds under mild reflux conditions. All the derivatives have been characterized through NMR, IR, and mass spectrometry.

In the ^{1}H NMR spectrum, the characteristic NH proton of the hydrazone moiety appears as a singlet around 10–11 ppm in DMSO-d_6 (**Fig. S21**) and as a broad peak near 8 ppm in $CDCl_3$ (**Fig. S15**), confirming the presence of the hydrazone proton. Additionally, the azomethine (–CH=N–) proton is observed as a distinct signal around 8.5 ppm, further supporting the formation of the hydrazone linkage. Aromatic protons resonate within the expected range of 7–9 ppm, while the methyl protons in compounds **3e** and **3f** appear at approximately 2.9 ppm and 3.8 ppm, respectively. The ^{13}C NMR spectrum shows a peak at approximately 175 ppm corresponding to the chromone carbonyl carbon, and the azomethine carbon is observed in the range of 140–150 ppm. Mass spectrometric analysis further confirmed the successful synthesis. For halogen-substituted compounds, distinct isotope patterns were observed: compounds **3b** and **3h** (containing chlorine) displayed characteristic M and M+2 peaks in a 3:1 ratio (**Fig. S6 and S18**), while compound **3c and 3g** (containing bromine) exhibited M and M+2 peaks in a 1:1 ratio (**Fig. S8 and S16**), consistent with the isotopic patterns of chlorine and bromine, respectively. All spectroscopic data are in agreement with the proposed structures and confirm the successful synthesis of the target hydrazone derivatives.

3.2. In-vitro studies

Reduced cell viability- Tamoxifen, 2 and **3a-j** significantly inhibited the cell viability of MCF-7 cells as compared to MDA-MB-231, determined by the MTT assay. The compounds **Tamoxifen, 2** and **3a-j** have not shown any adverse effect on HEK293 cells. The results demonstrated a significant, dose-dependent decrease in cell viability in both breast cancer cell lines as well as in the control cells. The half maximal inhibitory concentrations (IC_{50}) of **Tamoxifen, 2 and 3a-j** on MCF-7 cells were calculated to be ~27 μM ~57 μM, ~60 μM, ~42 μM, ~35 μM, ~55 μM, ~37 μM, ~57 μM, ~50 μM, ~45 μM, ~47 μM and ~30 μM (Fig. 2), for MDA-MB-231 the IC_{50} values were found to be ~57 μM, ~77 μM, ~81 μM, ~56 μM, ~47 μM, ~74 μM, ~50 μM, ~77 μM, ~67 μM, ~60 μM, ~63 μM and ~40 μM (Fig. 3) (Table 1), whereas, HEK293 cells showed no significant reduction in cell viability (Fig. 4). The cell morphology images of MCF-7 and MDA-MB-231 cell lines after the treatment with 50 μM of the given compounds are shown (Figs. 5 and 6.). This supports the hypothesis that these molecules selectively target estrogen receptor-positive (ER^+) breast cancer cells.

3.3. In-silico evaluation

3.3.1. Swiss-ADME properties

The Absorption, Distribution, Metabolism, and Excretion (ADME) properties of compounds **3a–j** revealed favourable pharmacokinetic and drug-like properties [61]. All derivatives complied with Lipinski's Rule of Five (MW < 500 Da, Log P ≤ 5, HBD ≤ 5, HBA ≤ 10) and Veber's criteria (RTB ≤ 10, TPSA ≤ 140 Å^2) (Tables 2 and 3), indicating strong potential for oral bioavailability [27,62,63]. Their water solubility (Log S ≥ –4) also indicates good absorption, and repeated bioavailability scores of 0.55 (55 %) and predictive models indicating F >10 % in rat experiments indicate favourable systemic exposure. All of the compounds had high GI absorption and BBB permeability, expanding their therapeutic potential. None of the derivatives contained any PAINS alerts [64], reducing the likelihood of false positives in biological tests. Synthetic accessibility scores (~3) validated that the compounds are easy to synthesize, sidestepping the intricacy that usually hinders lead development. Overall, these properties place the chromone-hydrazone derivatives as drug-like, pharmacokinetically favourable, and synthetically accessible scaffolds for further development in anti-cancer drug discovery.

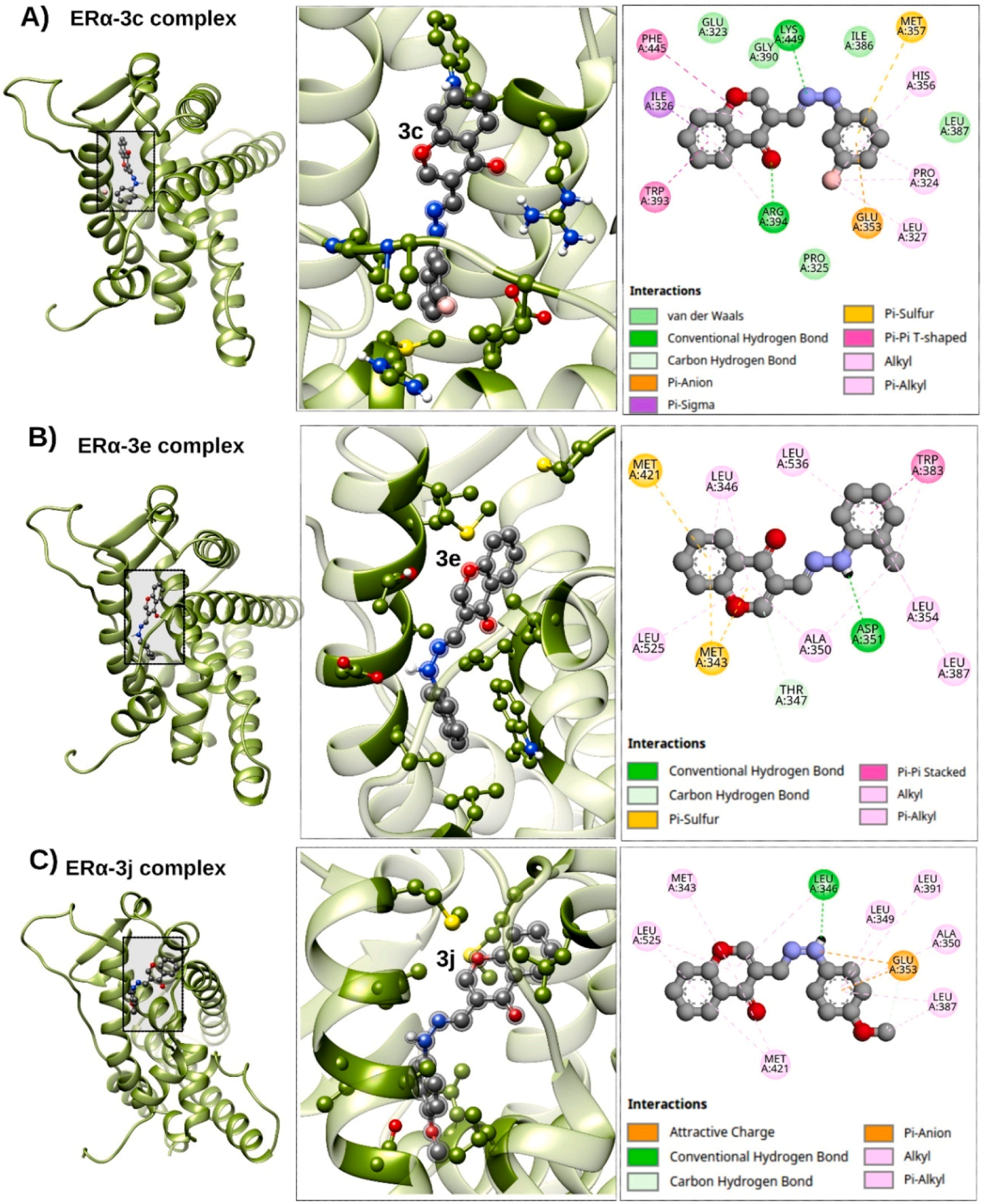

Fig. 9. Docked 3D and 2D representations of ERα in complex with compounds A) 3c, B) 3e, and C) 3j. In the 3D representation, ERα is shown in green cartoon representation, with interacting residues displayed in ball and stick format. The ligands 3c, 3e, and 3j are represented in grey ball and stick representation.

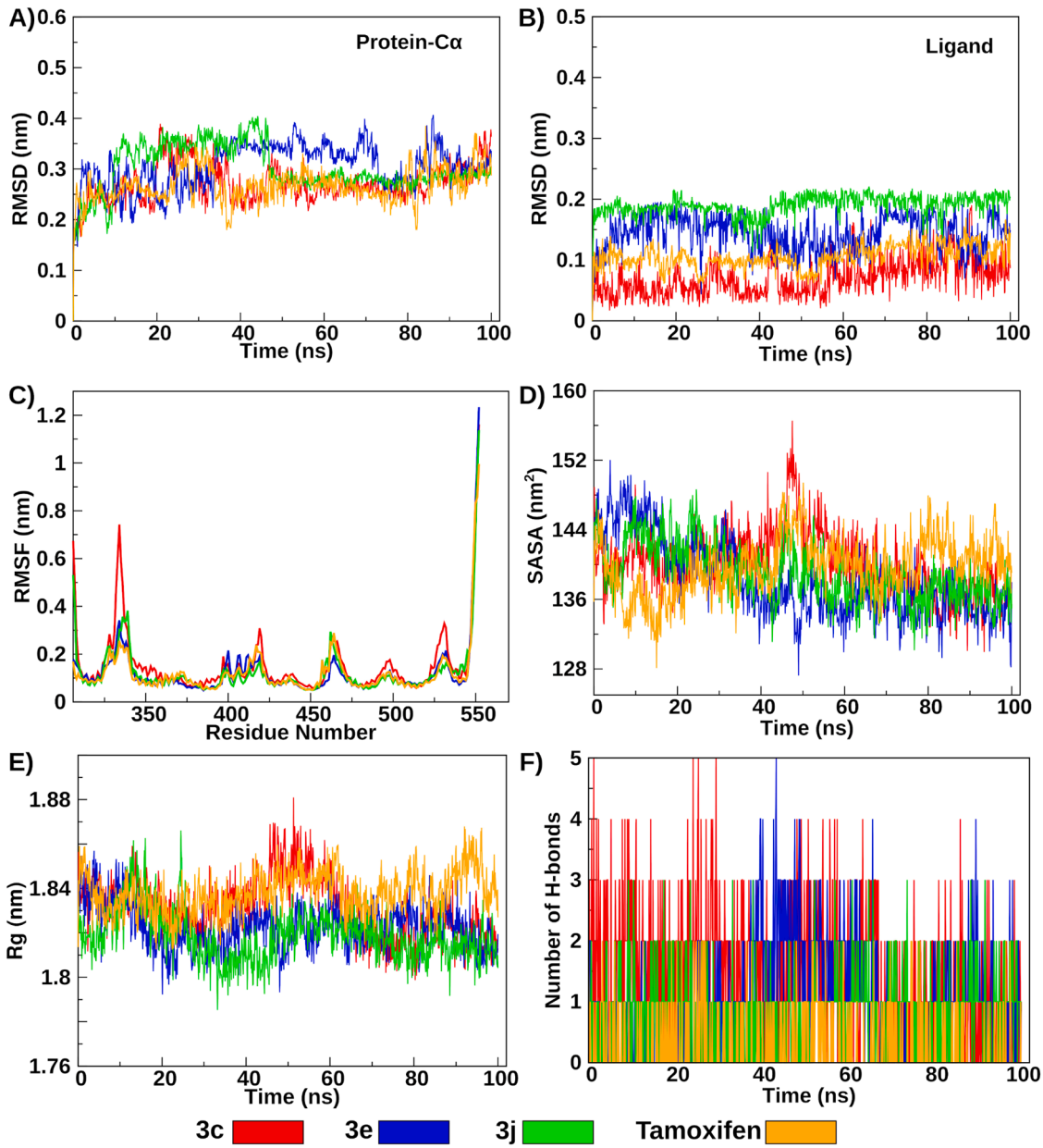

Fig. 10. A) RMSD plots of the ERα protein in complex with ligands 3c (red), 3e (blue), 3j (green), and Tamoxifen (orange). B) RMSD graphs of the individual ligands 3c, 3e, 3j, and Tamoxifen during the simulation. (C) RMSF plots showing residue-level fluctuations of ERα in each complex. (D) Solvent-accessible surface area (SASA) of ERα in the presence of each ligand. (E) Radius of gyration (Rg) of the ERα protein, indicating overall compactness of the complexes. (F) Hydrogen bond interactions between ligands 3c, 3e, 3j, and Tamoxifen with ERα over the simulation time.

3.3.2. Molecular docking

A molecular docking study was conducted using Auto Dock version 4.2.6, to investigate the binding interactions between the synthesized compounds **3a–j** and hormonal receptor - estrogen receptor alpha (ERα) (PDB ID: 3ERT), ERβ (PDB ID: 2FSZ), HER2 (PDB ID: 3PP0), and PR (PDB ID: 1A28). After docking, ER-alpha has been selected as a primary receptor because in hormone-positive breast cancer, ER-alpha plays a significant role. To avoid limiting the docking search to predefined active sites, blind docking was conducted by enclosing the entire protein within the grid box, without specifying a particular binding site [35]. Further, to validate the docking protocol, the co-crystallized ligand (hydroxytamoxifen) from the 3ERT structure was re-docked into its native binding site. The root-mean-square deviation (RMSD) between the docked and experimental poses was found to be 1.19 Å [36], confirming the reliability of the docking setup (Fig. 7).

The binding energy (BE) values of the **3a-3j** compounds with hormonal receptor complexes obtained from the docking studies are presented in Table 4. Compound **3j** emerged as the most potent inhibitor against MCF-7 breast cancer cell lines. Interestingly, despite its superior in vitro activity, it exhibited a slightly lower docking score (–7.29 kcal/mol). In contrast, compound **3c**, which achieved the best docking score (–8.20 kcal/mol) among the synthesized derivatives, demonstrated only the second-highest in vitro activity. The third most active compound, **3e**, showed a docking score of –7.47 kcal/mol. Several other compounds with relatively weaker inhibitory activity also displayed docking scores within a comparable range. These observations highlight a discrepancy between docking predictions and experimental results, suggesting that specific molecular interactions, beyond those captured in docking simulations, may contribute to the enhanced potency of compounds such as **3j** and **3e**.

Further analysis of the docking poses revealed that, despite the blind docking approach which allowed ligands to explore the entire protein

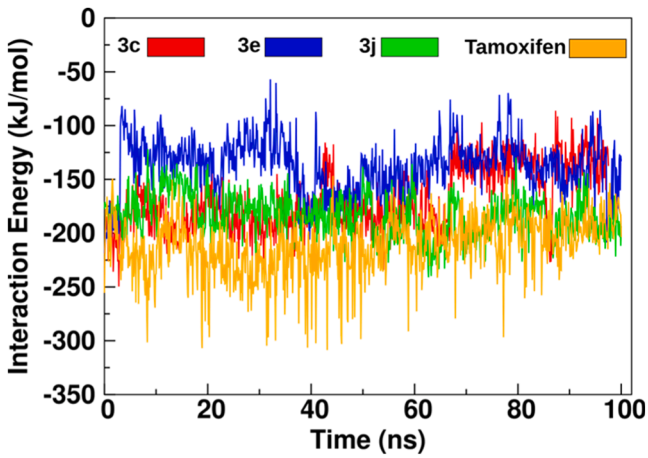

Fig. 11. The total non-bonded interaction energy (Coulombic and Van der Waals interaction) between the compounds (3c, 3e, 3j, and Tamoxifen) and ER-α.

Table 5
Quantum chemical properties of compounds 3c, 3e, and 3j calculated with the B3LYP functional and the 6-31G basis set.

Compound	3C	3e	3j
Ehomo (eV)	-5.7100	-5.2200	-5.1100
Elumo (eV)	-1.8300	-1.4600	-1.4200
Energy gap (eV)	3.8800	3.7600	3.6900
Ionization energy(I)	5.7100	5.2200	5.1100
Electron Affinity(A)	1.8300	1.4600	1.4200
Electronegativity(χ)	3.7700	3.3400	3.2650
Chemical Potential(μ)	-3.7700	-3.3400	-3.2650
Global hardness(η)	1.9400	1.8800	1.8450
Global softness(s)	0.5155	0.5319	0.5420
Electrophilicity index(ω)	3.6631	2.9669	2.8889

surface, compounds **3j** and **3e** consistently bound within the 17β-estradiol binding site (as defined in PDB ID: 1ERE) (Fig. 8A). In contrast, other ligands bound to alternative pockets (Fig. 8B). The specific binding of **3j** and **3e** to the estradiol-binding pocket suggests a competitive mode of action, potentially interfering with estradiol-induced signaling pathways that promote cancer cell proliferation [37,38]. Detailed key residue interactions were analyzed using BIOVIA Discovery Studio Visualizer, applying the default criteria specified in the software for each interaction type. Hydrogen bonds were defined by a donor–acceptor distance ≤ 3.4 Å and a donor-hydrogen-acceptor angle between 90°-180°. Alkyl interactions were identified using a maximum alkyl centroid distance of 5.5 Å, while π-alkyl and π-cation interactions were defined by an atom-π distance ≤ 5.0 Å with an angle cutoff of ≤ 40°. Based on these criteria, compound **3j** formed hydrogen bonds with Leu346 and engaged in alkyl and π-alkyl interactions with Leu387, Ala350, Leu391, Leu349, Met343, Met421, and Leu525 (Fig. 9B) If figure changes. Compound **3e** formed hydrogen bonds with Asp351 and Thr347, and alkyl/π-alkyl interactions with Leu346, Leu536, Leu354, Leu387, Ala350, and Leu525 (Fig. 9C). For comparison, Tamoxifen, a clinically used ERα inhibitor, exhibited a strong docking score of –10.93 kcal/mol (Table 4) within the estrogen-binding site, consistent with its experimentally determined high IC_{50} value.

3.3.3. Molecular dynamic simulation

To further investigate the stability of compounds **3c, 3e**, and **3j** with estrogen receptor alpha (ERα), 100 ns molecular dynamics (MD) simulations were performed. For comparison, the reference drug Tamoxifen in complex with ERα was also subjected to a 100 ns MD simulation. The resulting mD simulation trajectories were analyzed to calculate root-mean- square deviation (RMSD), root-mean-square fluctuation (RMSF), radius of gyration (Rg), solvent-accessible surface area (SASA), hydrogen bonding, and non-bonded interaction energies. The structural stability of the ERα core domain was evaluated using RMSD analysis. All four complexes (ERα-3j, ERα–3c, Erα-3e, and Erα-Tamoxifen) were shown to be stable with the RMSD within 0.4 nm during the simulation time (Fig. 10A). Further, ligand RMSD analysis confirmed that compounds **3j, 3c, 3e**, and Tamoxifen remained stable within the binding pocket, with RMSD values below 0.22 nm (Fig. 10B), indicating minimal deviation and consistent binding. Furthermore, to access the residue wise fluctuations, RMSF analysis were carried out (Fig. 10C), the result shows that the binding of compound **3c** induced increased fluctuations in the region containing the residues 330–340, suggesting localized conformational flexibility. The radius of gyration (Rg), used to evaluate the compactness of the protein-ligand complexes (Fig. 10D), indicated that the **ERα-3j** complex maintained the lowest Rg values, indicating greater overall compactness compared to **3c, 3e,** and Tamoxifen complex. SASA analysis revealed that all three complexes exhibited similar solvent exposure (Fig. 10E). Hydrogen bond analysis showed that all four ligands formed stable hydrogen bond interactions with ERα, persisting throughout the simulation and contributing to binding stability (Fig. 10F). Furthermore, non-bonded interaction energy calculations (van der Waals and Coulombic contributions) revealed that compound **3j** and the reference drug Tamoxifen exhibited the most favorable interaction energy with ERα, followed by **3e** and **3c** (Fig. 11). These findings suggest that compound **3j** exhibits strong binding affinity and structural stability within the ERα binding site, comparable to the reference drug Tamoxifen. Consistent with the MD results, **3j** also demonstrated notable activity against MCF-7 cells with an IC_{50} value of 30 μM, closely matching that of Tamoxifen (27 μM, control) (Table 1). Together, these results validate the simulation outcomes and highlight **3j** as a promising ERα inhibitor with therapeutic potential in estrogen receptor-positive cancers.

3.3.4. Density functional theory

3.3.4.1. Molecular orbital properties. DFT studies were conducted to explore the electronic and molecular properties of the most potent compounds- **3c, 3e**, and **3j**—against the MCF-7 breast cancer cell line.

Quantum chemical properties of compounds **3c, 3e**, and **3j** calculated with the B3LYP functional and the 6-31G basis set have been given in Table 5. The HOMO and LUMO energy levels, along with molecular orbital plots and band gaps, are presented in Fig. 12. Among them, compound **3j** exhibited the smallest HOMO–LUMO gap (3.69 eV), followed by **3e** (3.76 eV) and **3c** (3.88 eV) (Fig. 12 **A,** 12**C,** 12**D**), suggesting that **3j** has the highest chemical reactivity and electron transfer capability, potentially contributing to its superior biological activity.

3.3.4.2. Molecular electrostatic potential (MEP). To further identify potential sites for nucleophilic and electrophilic attacks, Molecular Electrostatic Potential (MESP) maps were generated for each compound. In the MESP plots, red regions indicate areas of high electron density (nucleophilic sites), while blue regions represent electron-deficient areas (electrophilic sites) [65]. Analysis of the MESP surfaces revealed that the chromone moiety contains highly nucleophilic oxygen atoms, followed by the imine nitrogen (Fig. 12B, 12D, 12F). These nucleophilic centers correspond well with the docking results, particularly in compound **3e**, which forms strong interactions with positively charged residues Lys449 and Asp394 (Fig. 12A). Furthermore, the presence of a methoxy group on the benzene ring in compound **3j** enhances its nucleophilic character (Fig. 12F), enabling more favorable interactions with the protein binding pocket. This characteristic may contribute to its higher binding stability in molecular dynamics simulations and its greater biological potency compared to **3e** and **3c**. Furthermore, the amino groups attached to the toluene moiety in **3e** (Fig. 12D) and the anisole moiety in **3j** exhibited higher electrophilic reactivity (Fig. 12F),

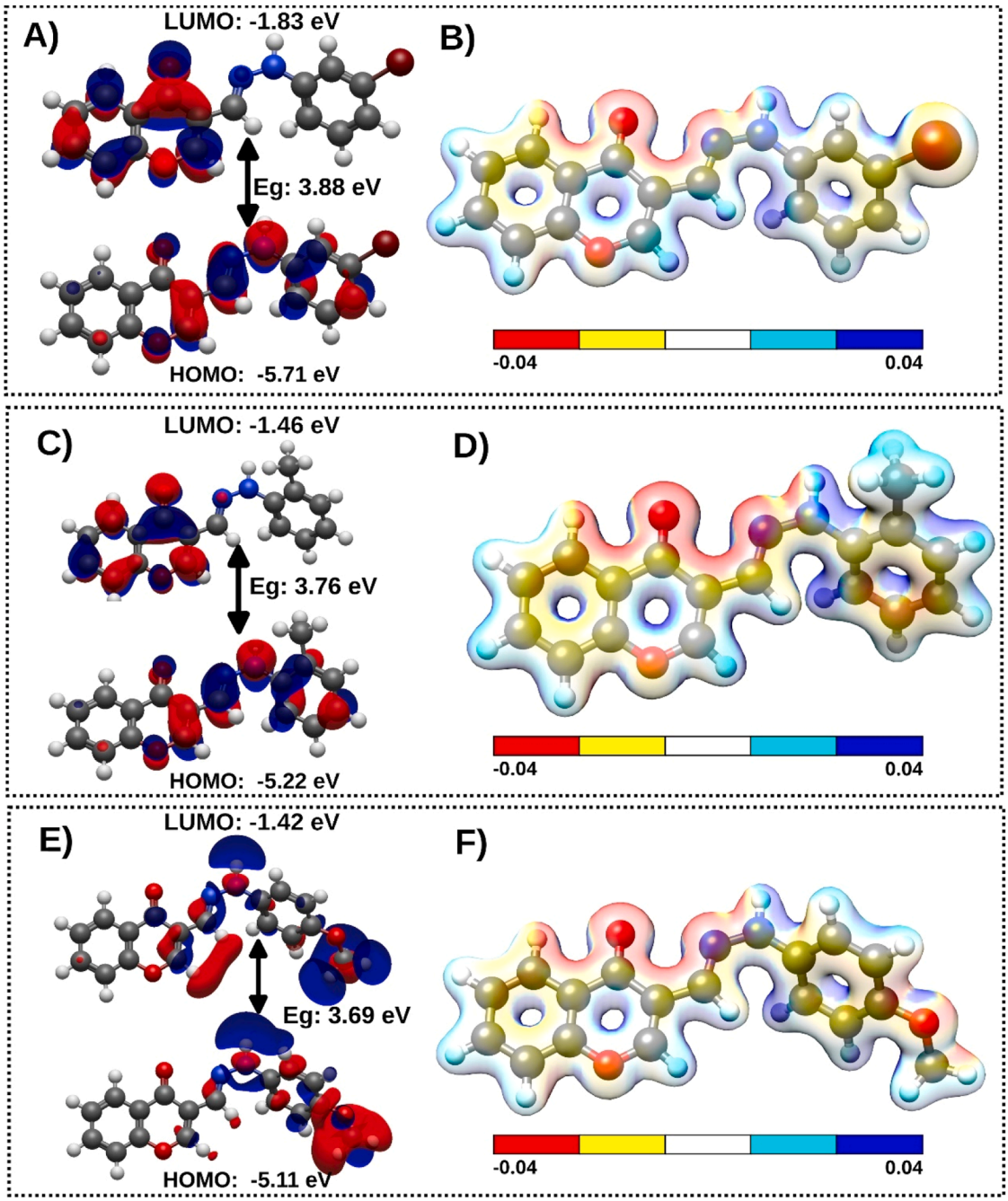

Fig. 12. The HOMO and LUMO of compound A) 3c C) 3e E) 3j. Molecular electrostatic potential (MEP) plots of compound B) 3c D) 3e F) 3j. Calculations were performed using the ORCA 6.0.1 program with the B3LYP functional and the 6-31G basis set.

as indicated by the deep blue regions in the MESP maps. These electrophilic centers were found to interact with residues Leu346 (Fig. 12C) and negatively charged Asp351 (Fig. 12B), suggesting a role in stabilizing the ligand–receptor complex. Notably, the electrophilic character of the toluene and anisole groups in **3e** and **3j**, respectively, was higher than that of the bromobenzene ring in **3c** (Fig. 12B, 12D, 12F). This differential electrophilic behavior may be responsible for the distinct binding site preferences observed in the docking studies: while **3e** and **3j** were found to bind within the estrogen binding site (similar to 17β-estradiol), **3c** appeared to occupy an alternative pocket (Fig. 8B).

The dual nucleophilic and electrophilic characteristics of compound **3j** may enhance its interactions with ERα, as evidenced by molecular dynamics simulations, thereby supporting its potential role as an inhibitor of the cancer cell line.

4. Structure activity relationship

The biological activity of chromone–hydrazone derivatives (**3a–j**) against ERα-positive breast cancer cells was rationalized through structural modifications, molecular docking, MD simulations, and quantum chemical descriptors. Substituent effects were critical. Electron-withdrawing groups (–CN, halogens) at ortho/para positions reduced activity by depleting electron density at the azomethine linkage and aromatic ring, thereby destabilizing hydrogen bonding and π–π interactions in the ERα pocket. Conversely, electron-donating groups (–OCH_3, –CH_3) enhanced resonance and conjugation, improving receptor affinity. Among halogenated analogues, the meta-bromo derivative outperformed meta-chloro and meta-fluoro due to bromine's lower electronegativity and larger radius, which favoured hydrophobic

contacts [66]. Methoxy substitution (**3j**) provided the optimal steric–electronic balance and showed the highest *in-vitro* potency. Docking predicted binding energies from –7.2 to –8.2 kcal/mol; compound **3c** had the best docking score (–8.20 kcal/mol) yet moderate in vitro activity, whereas **3j**, the most potent inhibitor, showed –7.29 kcal/mol. This mismatch highlights the limitations of docking scores and the importance of binding-site occupancy. Pose analysis revealed that active compounds **3j** and **3e** aligned within the canonical 17β-estradiol pocket, overlapping the native ligand, whereas other analogues (**3a, 3f, 3g, 3h, 3c**) localized in non-canonical cavities, reducing antagonism.

MD simulations (100 ns, NPT ensemble) supported these findings. The **ERα–3j** complex exhibited the lowest radius of gyration (Rg) and most favourable non-bonded interaction energies, reflecting compactness and stability compared with **ERα–3e, ERα–3c**, and **Tamoxifen**. Ligand RMSD traces showed **3j** remained stably confined in the pocket, closely mirroring Tamoxifen, suggesting its potential as a competitive ERα inhibitor. Quantum chemical descriptors further validated SAR trends. **3j** displayed the smallest HOMO–LUMO gap (3.69 eV), followed by **3e** (3.76 eV) and **3c** (3.88 eV), consistent with greater delocalization and reactivity. MEP mapping revealed electron-rich regions on the chromone carbonyl oxygen and methoxy groups of **3j**, facilitating interactions with Asp351 and Thr347, while its anisole moiety provided electrophilic character for additional stabilization. In **3e**, the amino-substituted toluene group engaged Leu346 and Asp351, whereas **3c**'s bromobenzene contributed weakly, causing alternate binding and less stability. The dual nucleophilic/electrophilic centers of **3j** likely enhanced complementarity, explaining its superior docking, MD stability, and *in-vitro* activity.

5. Conclusion

This research effectively designed, synthesized, and tested a new series of chromone–hydrazone derivatives (**3a–j**) as promising. ERα inhibitors with anti-breast cancer activity. Detailed characterization, docking, molecular dynamics simulations, and quantum chemical calculations revealed good structure–activity correlation, demonstrating the role of electronic substituents in affecting bioactivity. Among the tested compounds, **3j** emerged as the most promising lead, exhibiting the highest in vitro activity against ER-positive MCF-7 cells (IC_{50} = 30 μM), strong stability within the ERα binding pocket, and favorable pharmacokinetic properties (TPSA = 63.83 $Å^2$; log P = 2.78). Its methoxy group offered the best combination of electronic and steric effects that increased hydrogen bonding and hydrophobic interactions with key ERα residues. Computational descriptors also justified its greater reactivity, with the lowest HOMO–LUMO gap and optimal MEP distribution accounting for its increased biological activity and oral drug-likeness. Compound **3e** also showed excellent promise, coupling competitive binding to the traditional estradiol pocket with stable hydrogen-bonding interactions (Thr347, Asp351) and complementary hydrophobic contacts. Although less potent than **3j**, its electronic signature and reproducible stability in docking and MD simulations make it a promising secondary lead to optimize further. In summary, **3j** and **3e** are lead candidates as they exhibit selective ERα inhibition, acceptable pharmacokinetic properties, and strong experimental and computational support. These results present a solid foundation for furthering **3j** and **3e**, into more comprehensive preclinical studies as safe and potent anti-breast cancer drugs.

CRediT authorship contribution statement

Akrati Sant: Writing – original draft, Methodology, Formal analysis, Conceptualization. **Kavya K.M:** Software, Data curation. **Shama Parveen:** Visualization, Methodology, Data curation. **Ana Ahtsham:** Visualization, Data curation. **Krishnaveni S:** Visualization, Validation, Software. **Monisha Banerjee:** Visualization, Validation. **Sonika Bhatia:** Writing – review & editing, Supervision, Resources, Conceptualization.

Declaration of competing interest

The authors declared no conflict of interest.

Acknowledgements

The authors are grateful to the Department of Chemistry, Isabella Thoburn College, University of Lucknow, for providing Laboratory facilities. The authors would also like to thank SAIF-CDRI, Lucknow and Centre facility, BBAU, Lucknow for all the instrumentation facilities. Authors acknowledge the DBT-BUILDER and DST SERB Program, New Delhi, India and the Centre of Excellence scheme, Government of Uttar Pradesh, India, to facilitate cell culture in the Molecular and Human Genetics Laboratory, Department of Zoology, University of Lucknow, Lucknow. The authors also want to acknowledge the Department of Science and Technology (DST), Government of India, under the SERB-SURE project grant (Project No. SUR/2022/005410), for which Krishnaveni S., expresses their sincere gratitude. Kavya K. M. acknowledges the Department of Science and Technology (DST), Government of Karnataka, for financial support through the Karnataka DST-Ph.D. Fellowship.

Supplementary materials

Supplementary material associated with this article can be found, in the online version, at doi:10.1016/j.molstruc.2025.144636.

Data availability

Data will be made available on request.

References

[1] A.M. Filho, M. Laversanne, J. Ferlay, M. Colombet, M. Piñeros, A. Znaor, D. M. Parkin, I. Soerjomataram, F. Bray, The GLOBOCAN 2022 cancer estimates: Data sources, methods, and a snapshot of the cancer burden worldwide, Int. J. Cancer 156 (7) (2025) 1336–1346.

[2] G. Verma, A. Marella, M. Shaquiquzzaman, M. Akhtar, M.R. Ali, M.M. Alam, A review exploring biological activities of hydrazones, J. Pharm. Bioallied Sci. 6 (2) (2014).

[3] Edward, J. T.; Gauthier, M.; Chubb, F. L.; Ponka, P. J. J. o. C.; Data, E., Synthesis of new acylhydrazones as iron-chelating compounds. 1988, 33 (4), 538-540.

[4] I.C. Romao, S.M.C. Siqueira, F. Silva Abreu, H.S.D. Santos, Hydralazine and hydrazine derivatives: properties, applications, and repositioning potential, Chem. Biodivers. (2024) e202401561.

[5] Abdel-Aziz, H. A.; Aboul-Fadl, T.; Al-Obaid, A.-R. M.; Ghazzali, M.; Al-Dhfyan, A.; Contini, A. J. A. o. P. R., Design, synthesis and pharmacophoric model building of novel substituted nicotinic acid hydrazones with potential antiproliferative activity. 2012, 35, 1543-1552.

[6] de Oliveira, K. N.; Costa, P.; Santin, J. R.; Mazzambani, L.; Bürger, C.; Mora, C.; Nunes, R. J.; de Souza, M. M. J. B.; chemistry, m., Synthesis and antidepressant-like activity evaluation of sulphonamides and sulphonyl-hydrazones. 2011, 19 (14), 4295-4306.

[7] Chaston, T. B.; Richardson, D. R. J. A. j. o. h., Iron chelators for the treatment of iron overload disease: relationship between structure, redox activity, and toxicity. 2003, 73 (3), 200-210.

[8] V.T. Angelova, N.G. Vassilev, B. Nikolova-Mladenova, J. Vitas, R. Malbaša, G. Momekov, M. Djukic, L. Saso, Antiproliferative and antioxidative effects of novel hydrazone derivatives bearing coumarin and chromene moiety, Med. Chem. Res. 25 (9) (2016) 2082–2092.

[9] G. Wang, M. Chen, J. Wang, Y. Peng, L. Li, Z. Xie, B. Deng, S. Chen, W. Li, Synthesis, biological evaluation and molecular docking studies of chromone hydrazone derivatives as α-glucosidase inhibitors, Bioorg. Med. Chem. Lett. 27 (13) (2017) 2957–2961.

[10] A. Łazarenkow, J. Nawrot-Modranka, E. Brzezińska, U. Krajewska, M. Różalski, Synthesis, preliminary cytotoxicity evaluation of new 3-formylchromone hydrazones and phosphorohydrazone derivatives of coumarin and chromone, Med. Chem. Res. 21 (8) (2011) 1861–1868.

[11] Y. Fu, S. Zhou, Y. Liu, Y. Yang, X. Sun, C. Li, The cytotoxicity of benzaldehyde nitrogen mustard-2-pyridine carboxylic acid hydrazone being involved in topoisomerase IIalpha inhibition, Biomed. Res. Int. 2014 (1) (2014) 527042.

[12] Chaston, T. B.; Lovejoy, D. B.; Watts, R. N.; Richardson, D. R. J. C. c. r., Examination of the antiproliferative activity of iron chelators: multiple cellular targets and the different mechanism of action of triapine compared with desferrioxamine and the potent pyridoxal isonicotinoyl hydrazone analogue 311. 2003, 9 (1), 402-414.

[13] A. Sant, S. Modanwal, S. Parveen, A. Ahtsham, K. Porwal, N. Mishra, M. Banerjee, N. Chattopadhyay, A. Gupta, S. Bhatia, Value Addition to Citrus maxima Peels: Extraction and Modification of Naringenin into Hydrazones Derivatives for Anti-Breast Cancer and Osteogenic Activity via In Vitro and In Silico Studies, Chem. Biodivers. (2025) e01059.

[14] Lacy, A.; O'kennedy, R. J. C. p. d., Studies on coumarins and coumarin-related compounds to determine their therapeutic role in the treatment of cancer. 2004, 10 (30), 3797-3811.

[15] Jain, J.; Kumar, Y.; Sinha, R.; Kumar, R.; Stables, J. J. M. C., Menthone aryl acid hydrazones: a new class of anticonvulsants. 2011, 7 (1), 56-61.

[16] H.A. Abdel-Aziz, T. Elsaman, A. Al-Dhfyan, M.I. Attia, K.A. Al-Rashood, A.R. Al-Obaid, Synthesis and anticancer potential of certain novel 2-oxo-N'-(2-oxoindolin-3-ylidene)-2H-chromene-3-carbohydrazides, Eur. J. Med. Chem. 70 (2013) 358–363.

[17] Azizmohammadi, M.; Khoobi, M.; Ramazani, A.; Emami, S.; Zarrin, A.; Firuzi, O.; Miri, R.; Shafiee, A. J. E. j. o. m. c., 2H-chromene derivatives bearing thiazolidine-2, 4-dione, rhodanine or hydantoin moieties as potential anticancer agents. 2013, *59*, 15-22.

[18] Duan, Y.-d.; Jiang, Y.-y.; Guo, F.-x.; Chen, L.-x.; Xu, L.-l.; Zhang, W.; Liu, B. J. F., The antitumor activity of naturally occurring chromones: A review. 2019, 135, 114-129.

[19] Singh, P.; Kaur, M.; Holzer, W. J. E. j. o. m. c., Synthesis and evaluation of indole, pyrazole, chromone and pyrimidine based conjugates for tumor growth inhibitory activities–Development of highly efficacious cytotoxic agents. 2010, 45 (11), 4968-4982.

[20] Awadallah, F. M.; El-Waei, T. A.; Hanna, M. M.; Abbas, S. E.; Ceruso, M.; Oz, B. E.; Guler, O. O.; Supuran, C. T. J. E. j. o. m. c., Synthesis, carbonic anhydrase inhibition and cytotoxic activity of novel chromone-based sulfonamide derivatives. 2015, 96, 425-435.

[21] N.U.A. Mohsin, M. Irfan, S.U. Hassan, U. Saleem, Current strategies in development of new chromone derivatives with diversified pharmacological activities: a review, Pharm. Chem. J. 54 (3) (2020) 241–257.

[22] H.K. Koul, M. Pal, S. Koul, Role of p38 MAP Kinase Signal Transduction in Solid Tumors, Genes. Cancer 4 (9-10) (2013) 342–359.

[23] H.M. Abo-Salem, S.S.M. El Souda, H.I. Shafey, K.M.A. Zoheir, K.M. Ahmed, K. Mahmoud, K.F. Mahrous, N.M. Fawzy, Synthesis, bioactivity assessment, molecular docking and ADMET studies of new chromone congeners exhibiting potent anticancer activity, Sci. Rep. 14 (1) (2024) 9636.

[24] L. Kaviarasan, B. Gowramma, R. Kalirajan, M. Mevithra, S. Chandralekha, Molecular docking studies and synthesis of a new class of chroman-4-one fused 1,3,4-thiadiazole derivatives and evaluation for their anticancer potential, J. Iran. Chem. Soc. 17 (8) (2020) 2083–2094.

[25] M.S. Galla, N.B. Kale, A. Sharma, A. Hajare, C. Godugu, N. Shankaraiah, Development of chromone-thiazolidine-2,4-dione Knoevenagel conjugates as apoptosis inducing agents, Bioorg. Med. Chem. Lett. 109 (2024) 129853.

[26] S. Parveen, S. Kumar, S. Pal, N.P. Yadav, J. Rajawat, M. Banerjee, Enhanced therapeutic efficacy of Piperlongumine for cancer treatment using nano-liposomes mediated delivery, Int. J. Pharm. 643 (2023) 123212.

[27] F. Ghous, S. Rai, S. Kumar, M. Banerjee, A. Bishnoi, Synthesis, in-Silico investigations, molecular docking, ADMET, and anti-lung cancer activity studies of 1,2,4,5-tetraazaspiro[5.5]undecane-3-thione, Chem. Phys. 574 (2023).

[28] M.M. Hasan, Z. Khan, M.S. Chowdhury, M.A. Khan, M.A. Moni, M.H. Rahman, In silico molecular docking and ADME/T analysis of Quercetin compound with its evaluation of broad-spectrum therapeutic potential against particular diseases, Inform. Med. Unlocked 29 (2022) 100894.

[29] T.U. Consortium, The Universal Protein Resource (UniProt), Nucleic Acids Res. 36 (suppl_1) (2007) D190–D195.

[30] H. Berman, K. Henrick, H. Nakamura, Announcing the worldwide protein data bank, Nat. Struct. Biol. 10 (12) (2003) 980.

[31] Morris, G. M.; Huey, R.; Lindstrom, W.; Sanner, M. F.; Belew, R. K.; Goodsell, D. S.; Olson, A. J., AutoDock4 and AutoDockTools4: Automated docking with selective receptor flexibility. 2009, 30 (16), 2785-2791.

[32] D.S. Goodsell, G.M. Morris, A.J. Olson, Automated docking of flexible ligands: applications of AutoDock, J. Mol. Recognit. : JMR 9 (1) (1996) 1–5.

[33] M.J. Abraham, T. Murtola, R. Schulz, S. Páll, J.C. Smith, B. Hess, E. Lindahl, GROMACS: High performance molecular simulations through multi-level parallelism from laptops to supercomputers, SoftwareX. 1-2 (2015) 19–25.

[34] S. Páll, A. Zhmurov, P. Bauer, M. Abraham, M. Lundborg, A. Gray, B. Hess, E. Lindahl, Heterogeneous parallelization and acceleration of molecular dynamics simulations in GROMACS, J. Chem. Phys. 153 (13) (2020) 134110.

[35] H.J.C. Berendsen, D. van der Spoel, R. van Drunen, GROMACS: A message-passing parallel molecular dynamics implementation, Comput. Phys. Commun. 91 (1) (1995) 43–56.

[36] J. Lemkul, From proteins to perturbed hamiltonians: a suite of tutorials for the GROMACS-2018 molecular simulation package [Article v1.0], Living J. Comput. Mol. Sci. 1 (2018).

[37] U. N, K. S, Molecular dynamics simulation study on Thermotoga maritima EngA: GTP/GDP bound state of the second G-domain influences the domain-domain interface interactions, J. Biomol. Struct. Dyn. 40 (3) (2022) 1387–1399.

[38] M.K. K, U. N, K. S, Conformational dynamics and ribosomal interactions of Bacillus subtilis Obg in various nucleotide-bound states: Insights from molecular dynamics simulation, Int. J. Biol. Macromol. 279 (2024) 135337.

[39] A. Pandith, U. Nagarajachari, R.K.G. Siddappa, S. Lee, C.J. Park, K. Sannathammegowda, Y.J. Seo, Loop-mediated fluorescent probes for selective discrimination of parallel and antiparallel G-Quadruplexes, Bioorg. Med. Chem. 35 (2021) 116077.

[40] E.F. Pettersen, T.D. Goddard, C.C. Huang, G.S. Couch, D.M. Greenblatt, E.C. Meng, T.E. Ferrin, UCSF Chimera—A visualization system for exploratory research and analysis, J. Comput. Chem. 25 (13) (2004) 1605–1612.

[41] J. Huang, S. Rauscher, G. Nawrocki, T. Ran, M. Feig, B.L. de Groot, H. Grubmüller, A.D. MacKerell, CHARMM36m: an improved force field for folded and intrinsically disordered proteins, Nat. Methods 14 (1) (2017) 71–73.

[42] B.R. Brooks, C.L. Brooks 3rd, A.D. Mackerell Jr., L. Nilsson, R.J. Petrella, B. Roux, Y. Won, G. Archontis, C. Bartels, S. Boresch, A. Caflisch, L. Caves, Q. Cui, A. R. Dinner, M. Feig, S. Fischer, J. Gao, M. Hodoscek, W. Im, K. Kuczera, T. Lazaridis, J. Ma, V. Ovchinnikov, E. Paci, R.W. Pastor, C.B. Post, J.Z. Pu, M. Schaefer, B. Tidor, R.M. Venable, H.L. Woodcock, X. Wu, W. Yang, D.M. York, M. Karplus, CHARMM: the biomolecular simulation program, J. Comput. Chem. 30 (10) (2009) 1545–1614.

[43] MacKerell Jr., A. D.; Brooks, B.; Brooks III, C. L.; Nilsson, L.; Roux, B.; Won, Y.; Karplus, M., CHARMM: The Energy Function and Its Parameterization. In *Encycl. Comput. Chem.*, 1998.

[44] Oostenbrink, C.; Villa, A.; Mark, A. E.; Van Gunsteren, W. F., A biomolecular force field based on the free enthalpy of hydration and solvation: The GROMOS force-field parameter sets 53A5 and 53A6. 2004, 25 (13), 1656-1676.

[45] K. Vanommeslaeghe, E. Hatcher, C. Acharya, S. Kundu, S. Zhong, J. Shim, E. Darian, O. Guvench, P. Lopes, I. Vorobyov, A.D. Mackerell Jr., CHARMM general force field: A force field for drug-like molecules compatible with the CHARMM all-atom additive biological force fields, J. Comput. Chem. 31 (4) (2010) 671–690.

[46] K. Vanommeslaeghe, A.D. MacKerell Jr., Automation of the CHARMM General Force Field (CGenFF) I: bond perception and atom typing, J. Chem. Inf. Model. 52 (12) (2012) 3144–3154.

[47] D.J. Price, C.L. Brooks III, A modified TIP3P water potential for simulation with Ewald summation, J. Chem. Phys. 121 (20) (2004) 10096–10103.

[48] W. Jorgensen, J. Chandrasekhar, J. Madura, R. Impey, M. Klein, Comparison of Simple Potential Functions for Simulating Liquid Water, J. Chem. Phys 79 (1983) 926–935.

[49] G. Bussi, D. Donadio, M. Parrinello, Canonical sampling through velocity rescaling, J. Chem. Phys. 126 (1) (2007) 014101.

[50] M. Parrinello, A. Rahman, Polymorphic transitions in single crystals: A new molecular dynamics method, J. Appl. Phys. 52 (12) (1981) 7182–7190.

[51] T. Darden, D. York, L. Pedersen, Particle mesh Ewald: An N·log(N) method for Ewald sums in large systems, J. Chem. Phys. 98 (12) (1993) 10089–10092.

[52] U. Essmann, L. Perera, M. Berkowitz, T. Darden, H. Lee, L. Pedersen, A Smooth particle mesh Ewald method, J. Chem. Phys 103 (1995) 8577.

[53] Hess, B.; Bekker, H.; Berendsen, H. J. C.; Fraaije, J. G. E. M., LINCS: A linear constraint solver for molecular simulations. 1997, 18 (12), 1463-1472.

[54] N, U.; K M. K.; S, K., Molecular dynamics simulation studies on Bacillus subtilis RbgA: insights into the RbgA-ribosome association and GTPase activity. *J. Biomol. Struct. Dyn.*, 1-11.

[55] W. Humphrey, A. Dalke, K. Schulten, VMD: visual molecular dynamics, J. Mol. Graph. 14 (1) (1996) 27–28, 33-8.

[56] Z. Yang, K. Lasker, D. Schneidman-Duhovny, B. Webb, C.C. Huang, E.F. Pettersen, T.D. Goddard, E.C. Meng, A. Sali, T.E. Ferrin, UCSF Chimera, MODELLER, and IMP: an integrated modeling system, J. Struct. Biol. 179 (3) (2012) 269–278.

[57] F. Neese, F. Wennmohs, U. Becker, C. Riplinger, The ORCA quantum chemistry program package, J. Chem. Phys. 152 (2020) 224108.

[58] A.D. Becke, A new mixing of Hartree–Fock and local density-functional theories, J. Chem. Phys. 98 (2) (1993) 1372–1377.

[59] W.J. Hehre, Ab initio molecular orbital theory, Acc. Chem. Res. 9 (11) (1976) 399–406.

[60] M.D. Hanwell, D.E. Curtis, D.C. Lonie, T. Vandermeersch, E. Zurek, G.R. Hutchison, Avogadro: an advanced semantic chemical editor, visualization, and analysis platform, J. Cheminformatics 4 (1) (2012) 17.

[61] F. Ghous, S. Shukla, R. Singh, S. Parveen, M. Banerjee, A. Bishnoi, Synthesis, crystal structure, computational investigation, molecular docking analysis and anti-lung cancer activity of novel (Z)-3-amino-2-(cyclohexylidenehydrazono)thiazolidin-4-one, J. Mol. Struct. 1285 (2023).

[62] D.F. Veber, S.R. Johnson, H.-Y. Cheng, B.R. Smith, K.W. Ward, K.D. Kopple, Molecular Properties That Influence the Oral Bioavailability of Drug Candidates, J. Med. Chem. 45 (12) (2002) 2615–2623.

[63] S. Rai, A. Bishnoi, S. Fatma, S. Shukla, P. Devi, V.J.P.A.C. Singh, An Expedient Three-component Synthesis of Novel Pyrido-pyrimidine Derivatives: Antimicrobial Activity, Mol. Docking ADME Stud. 44 (4) (2024) 2752–2774.

[64] T. Erdogan, DFT, molecular docking and molecular dynamics simulation studies on some newly introduced natural products for their potential use against SARS-CoV-2, J. Mol. Struct. 1242 (2021) 130733.

[65] H.K. Nagaraja rao, B. Poojary, K.K. Mohan Kumar, G. Chandrasehar, K. Sannathammegowda, A. Pandith, Novel Isoxazolylpyrimidine Derivatives: Design, Synthesis, Antifungal Activity and In-Silico Studies, Asian J. Org. Chem. 13 (5) (2024) e202400021.

[66] S. Kortagere, S. Ekins, W.J. Welsh, Halogenated ligands and their interactions with amino acids: Implications for structure–activity and structure–toxicity relationships, J. Mol. Graph. Model. 27 (2) (2008) 170–177.